The Herschel census of infrared SEDs through cosmic time

E. Le Floc'H, S. Lilly, J. S. Kartaltepe, B. Magnelli, G. Magdis, L. Marchetti, H. T. Nguyen, R. Nordon, B. O'Halloran, S. J. Oliver, et al.

Monthly Notices
of the
ROYAL ASTRONOMICAL SOCIETY

MNRAS **431,** 2317–2340 (2013) doi:10.1093/mnras/stt330
Advance Access publication 2013 April 1

The *Herschel* census of infrared SEDs through cosmic time★

M. Symeonidis,[1]† M. Vaccari,[2,3] S. Berta,[4] M. J. Page,[1] D. Lutz,[4] V. Arumugam,[5] H. Aussel,[6] J. Bock,[7,8] A. Boselli,[6] V. Buat,[9] P. L. Capak,[7] D. L. Clements,[10] A. Conley,[11] L. Conversi,[12] A. Cooray,[7,13] C. D. Dowell,[7,8] D. Farrah,[14] A. Franceschini,[2] E. Giovannoli,[3] J. Glenn,[11,15] M. Griffin,[16] E. Hatziminaoglou,[17] H.-S. Hwang,[18] E. Ibar,[19] O. Ilbert,[20] R. J. Ivison,[5,19] E. Le Floc'h,[6] S. Lilly,[21] J. S. Kartaltepe,[22] B. Magnelli,[4] G. Magdis,[23] L. Marchetti,[2] H. T. Nguyen,[7,8] R. Nordon,[24] B. O'Halloran,[10] S. J. Oliver,[25] A. Omont,[26] A. Papageorgiou,[16] H. Patel,[10] C. P. Pearson,[27,28] I. Pérez-Fournon,[29,30] M. Pohlen,[16] P. Popesso,[4] F. Pozzi,[31] D. Rigopoulou,[23,27] L. Riguccini,[32] D. Rosario,[4] I. G. Roseboom,[5] M. Rowan-Robinson,[10] M. Salvato,[33] B. Schulz,[7,34] Douglas Scott,[35] N. Seymour,[36] D. L. Shupe,[7,34] A. J. Smith,[25] I. Valtchanov,[12] L. Wang,[25] C. K. Xu,[7,34] M. Zemcov[7,8] and S. Wuyts[4]

[1]*Mullard Space Science Laboratory, University College London, Holmbury St. Mary, Dorking, Surrey RH5 6NT, UK*
[2]*Dipartimento di Astronomia, Università di Padova, vicolo Osservatorio, 3, I-35122 Padova, Italy*
[3]*Astrophysics Group, Physics Department, University of the Western Cape, Private Bag X17, 7535, Bellville, Cape Town, South Africa*
[4]*Max-Planck-Institut für Extraterrestrische Physik (MPE), Postfach 1312, D-85741 Garching, Germany*
[5]*Institute for Astronomy, Blackford Hill, Edinburgh EH9 3HJ, UK*
[6]*Laboratoire AIM-Paris-Saclay, CEA/DSM/Irfu – CNRS – Université Paris Diderot, CE-Saclay, pt courrier 131, F-91191 Gif-sur-Yvette, France*
[7]*California Institute of Technology, 1200 E. California Blvd., Pasadena, CA 91125, USA*
[8]*Jet Propulsion Laboratory, 4800 Oak Grove Drive, Pasadena, CA 91109, USA*
[9]*Laboratoire d'Astrophysique de Marseille, OAMP, Université Aix-marseille, CNRS, 38 rue Frédéric Joliot-Curie, F-13388 Marseille cedex 13, France*
[10]*Astrophysics Group, Imperial College London, Blackett Laboratory, Prince Consort Road, London SW7 2AZ, UK*
[11]*Center for Astrophysics and Space Astronomy 389-UCB, University of Colorado, Boulder, CO 80309, USA*
[12]*Herschel Science Centre, European Space Astronomy Centre, Villanueva de la Cañada, E-28691 Madrid, Spain*
[13]*Department of Physics & Astronomy, University of California, Irvine, CA 92697, USA*
[14]*Department of Physics, Virginia Tech, Blacksburg, VA 24061, USA*
[15]*Department of Astrophysical and Planetary Sciences, CASA 389-UCB, University of Colorado, Boulder, CO 80309, USA*
[16]*School of Physics and Astronomy, Cardiff University, Queens Buildings, The Parade, Cardiff CF24 3AA, UK*
[17]*ESO, Karl-Schwarzschild-Str. 2, D-85748 Garching bei München, Germany*
[18]*Smithsonian Astrophysical Observatory, 60 Garden Street, Cambridge, MA 02138, USA*
[19]*UK Astronomy Technology Centre, Royal Observatory, Blackford Hill, Edinburgh EH9 3HJ, UK*
[20]*Laboratoire dAstrophysique de Marseille, Universite de Provence, CNRS, BP 8, Traverse du Siphon, F-13376 Marseille Cedex 12, France*
[21]*Institute for Astronomy, Wolfgang-Pauli-Strasse 27, CH-8093 Zurich, Switzerland*
[22]*National Optical Astronomy Observatory, 950 N. Cherry Ave, Tucson, AZ 85719, US*
[23]*Department of Astrophysics, University of Oxford, Denys Wilkinson Building, Keble Road, Oxford OX1 3RH, UK*
[24]*School of Physics and Astronomy, The Raymond and Beverly Sackler Faculty of Exact Sciences, Tel-Aviv University, Tel-Aviv 69978, Israel*
[25]*Astronomy Centre, Department of Physics & Astronomy, University of Sussex, Brighton BN1 9QH, UK*
[26]*Institut d'Astrophysique de Paris, UMR 7095, CNRS, UPMC Univ. Paris 06, 98bis boulevard Arago, F-75014 Paris, France*
[27]*RAL Space, Rutherford Appleton Laboratory, Chilton, Didcot, Oxfordshire OX11 0QX, UK*
[28]*Institute for Space Imaging Science, University of Lethbridge, Lethbridge, Alberta, T1K 3M4, Canada*
[29]*Instituto de Astrofísica de Canarias (IAC), E-38200 La Laguna, Tenerife, Spain*
[30]*Departamento de Astrofísica, Universidad de La Laguna (ULL), E-38205 La Laguna, Tenerife, Spain*
[31]*INAF–Osservatorio Astronomico di Roma, via di Franscati 33, I-00040 Monte Porzio Catone, Italy*
[32]*Astrophysics Branch, NASA/Ames Research Center, MS 245-6, Moffett Field, CA 94035, USA*
[33]*Max-Planck-Institut fur extraterrestrische Physik, Giessenbachstrasse 1, D-85748 Garching, Germany*

★ *Herschel* is an ESA space observatory with science instruments provided by European-led Principal Investigator consortia and with important participation from NASA.

† E-mail: m.symeonidis@ucl.ac.uk

[34] *Infrared Processing and Analysis Center, MS 100-22, California Institute of Technology, JPL, Pasadena, CA 91125, USA*
[35] *Department of Physics & Astronomy, University of British Columbia, 6224 Agricultural Road, Vancouver, BC V6T 1Z1, Canada*
[36] *CSIRO Astronomy & Space Science, PO Box 76, Epping, NSW 1710, Australia*

Accepted 2013 February 19. Received 2013 February 4; in original form 2012 October 21

ABSTRACT

Using *Herschel* data from the deepest SPIRE and PACS surveys (HerMES and PEP) in COSMOS, GOODS-S and GOODS-N, we examine the dust properties of infrared (IR)-luminous ($L_{\rm IR} > 10^{10}$ L$_\odot$) galaxies at $0.1 < z < 2$ and determine how these evolve with cosmic time. The unique angle of this work is the rigorous analysis of survey selection effects, making this the first study of the star-formation-dominated, IR-luminous population within a framework almost entirely free of selection biases. We find that IR-luminous galaxies have spectral energy distributions (SEDs) with broad far-IR peaks characterized by cool/extended dust emission and average dust temperatures in the 25–45 K range. Hot ($T > 45$ K) SEDs and cold ($T < 25$ K), cirrus-dominated SEDs are rare, with most sources being within the range occupied by warm starbursts such as M82 and cool spirals such as M51. We observe a luminosity–temperature ($L-T$) relation, where the average dust temperature of log [$L_{\rm IR}$/L$_\odot$] $\sim$ 12.5 galaxies is about 10 K higher than that of their log [$L_{\rm IR}$/L$_\odot$] $\sim$ 10.5 counterparts. However, although the increased dust heating in more luminous systems is the driving factor behind the $L-T$ relation, the increase in dust mass and/or starburst size with luminosity plays a dominant role in shaping it. Our results show that the dust conditions in IR-luminous sources evolve with cosmic time: at high redshift, dust temperatures are on average up to 10 K lower than what is measured locally ($z \lesssim 0.1$). This is manifested as a flattening of the $L-T$ relation, suggesting that (ultra)luminous infrared galaxies [(U)LIRGs] in the early Universe are typically characterized by a more extended dust distribution and/or higher dust masses than local equivalent sources. Interestingly, the evolution in dust temperature is luminosity dependent, with the fraction of LIRGs with $T < 35$ K showing a two-fold increase from $z \sim 0$ to $z \sim 2$, whereas that of ULIRGs with $T < 35$ K shows a six-fold increase. Our results suggest a greater diversity in the IR-luminous population at high redshift, particularly for ULIRGs.

Key words: galaxies: evolution – galaxies: high-redshift – galaxies: starburst – infrared: galaxies – submillimetre: galaxies.

1 INTRODUCTION

The discovery of a class of infrared (IR)-luminous ($L_{\rm IR} > 10^{10}$ L$_\odot$) galaxies in the 1960s (e.g. Johnson 1966; Low & Tucker 1968; Kleinmann & Low 1970), followed by the detection of the cosmic infrared background (Puget et al. 1996; Hauser et al. 1998) unfolded a new era in extragalactic astronomy. Infrared/submm surveys with *IRAS* (Neugebauer et al. 1984), *ISO* (Kessler et al. 1996), JCMT/SCUBA (Holland et al. 1999), *Spitzer* (Werner et al. 2004) and *AKARI* (Murakami et al. 2007) revealed that the early Universe was more active than previously thought, uncovering a large number of dust-enshrouded galaxies whose bolometric luminosity emerges almost entirely in the infrared (e.g. Soifer et al. 1984a; Lutz et al. 1996, 2005; Sanders & Mirabel 1996; Rowan-Robinson et al. 1997, 2005; Lisenfeld, Isaak & Hills 2000; Goto et al. 2010, and many more). These IR-luminous galaxies are rare in the local Universe (e.g. Kim & Sanders 1998) but exhibit a strong increase in number density at earlier epochs (e.g. Takeuchi, Buat & Burgarella 2005), being responsible for about half the total light emitted from all galaxies integrated through cosmic time (e.g. Gispert, Lagache & Puget 2000; Lagache, Puget & Dole 2005; Dole et al. 2006). The abundance of these sources at high redshifts ($z \sim$ 1–4; e.g. Hughes et al. 1998; Eales et al. 1999, 2000; Blain et al. 2004; Le Floc'h et al. 2004; Schinnerer et al. 2008; Pannella et al. 2009) indicates that they started forming very early in cosmic history, potentially challenging the hierarchical paradigm of Λ cold dark matter (CDM; e.g. Granato et al. 2004; Baugh et al. 2005; Bower et al. 2006; Somerville et al. 2008).

IR-luminous galaxies are the ideal laboratories for studies of galaxy formation and evolution through chemical enrichment, star formation, black hole accretion and stellar mass build-up. They hide an immensely active interstellar medium (e.g. Lutz et al. 1998; Farrah et al. 2003; Narayanan et al. 2005; Sturm et al. 2010) and are the ultimate stellar nurseries, with star-formation rates (SFRs) up to a few thousand times higher than Milky Way-type galaxies (e.g. Kennicutt 1998; Egami et al. 2004; Choi et al. 2006; Rieke et al. 2009). In addition, they are amongst the most massive galaxies in the Universe (e.g. Dye et al. 2008; Michałowski, Hjorth & Watson 2010) and often their morphologies show signs of interactions and mergers (e.g. Sanders & Mirabel 1996; Farrah et al. 2001, 2002; Moustakas et al. 2004; Kartaltepe et al. 2010b). Finally, they frequently harbour an active galactic nucleus (AGN), which is commonly considered a key player in the evolution of the system (e.g. Genzel et al. 1998; Ptak et al. 2003; Alexander et al. 2005; Page et al. 2012).

Until recently our view of the IR-luminous galaxy population at high redshift has been based on data from the space observatories *ISO* and *Spitzer*, as well as ground-based submm/mm facilities such as JCMT/SCUBA, APEX/LABOCA, IRAM/MAMBO and SMA/AzTEC. Although huge advances have been made in our understanding of the nature and evolution of these sources, it has been challenging to reconcile the data from space observatories with comparable ground-based IR/mm data sets. In recent years, it has become increasingly apparent that, besides strong evolution in IR galaxy number density (e.g. Le Floc'h et al. 2005; Huynh et al. 2007; Magnelli et al. 2009; Berta et al. 2010, 2011), the physical properties of IR galaxies might also evolve with time, with the rate of evolution potentially changing as a function of luminosity (Seymour et al. 2010). Studies of the local Universe showed that ultraluminous infrared galaxies (ULIRGs) are characterized by warm average dust temperatures (e.g. Soifer et al. 1984b; Klaas et al. 1997; Clements, Dunne & Eales 2010), strong silicate absorption and polycyclic aromatic hydrocarbon (PAH) emission features in their mid-IR continuum (e.g., Brandl et al. 2006; Armus et al. 2007), as well as compact starburst sizes (e.g. Condon et al. 1991; Soifer et al. 2001). However, with the onset of submm/mm facilities which probed the early Universe ($z > 2$), such as SCUBA in the late 1990s, a different picture emerged. Many IR-luminous galaxies at high redshift were found to be less compact than their local counterparts (e.g. Tacconi et al. 2006; Iono et al. 2009; Rujopakarn et al. 2011), exhibiting stronger PAH emission (Farrah et al. 2007, 2008; Valiante et al. 2007) and a greater abundance of cold dust (Kovács et al. 2006; Pope et al. 2006; Coppin et al. 2008). It was later shown that these differences in the measured dust properties were partly due to selection effects and partly due to evolution (Symeonidis et al. 2009, 2011a). Moreover, the exploitation of long-wavelength data from *ISO* (Rowan-Robinson et al. 2005) and *Spitzer* (Symeonidis et al. 2008) enabled the discovery of IR-luminous galaxies at $z < 1$, with a spectrum of properties which overlapped with both the local population and the SCUBA-detected, $z > 2$, sources, providing the missing link between the two (Symeonidis et al. 2009).

The launch of the *Herschel Space Observatory*[1] (Pilbratt et al. 2010) has opened a new window in infrared astronomy, as it is the only facility to date and for the foreseeable future to perfectly span the wavelength range in which most of the Universe's obscured radiation emerges (70–500 μm), uncovering unprecedented numbers of dust-enshrouded galaxies over a sizeable fraction of cosmic time. The large dynamical range of the Photodetector Array Camera and Spectrometer (PACS; Poglitsch et al. 2010) and the Spectral and Photometric Imaging Receiver (SPIRE; Griffin et al. 2010) instruments has enabled spectral energy distributions (SEDs) to be compiled for a large range of objects, both for AGN (e.g. Hatziminaoglou et al. 2010; Seymour et al. 2011) and star-forming galaxies (e.g. Rowan-Robinson et al. 2010). Recent studies of the properties of the IR-luminous galaxy population using *Herschel* data provide an excellent showcase of the capabilities of this observatory (some examples from the multitude of *Herschel* papers on this topic: Amblard et al. 2010; Buat et al. 2010; Berta et al. 2010, 2011; Dye et al. 2010; Eales et al. 2010b; Gruppioni et al. 2010; Hwang et al. 2010; Ivison et al. 2010; Magdis et al. 2010, 2011; Magnelli et al. 2010, 2012; Rodighiero et al. 2010; Rowan-Robinson et al. 2010; Dunne et al. 2011; Symeonidis, Page & Seymour 2011b; Kartaltepe et al. 2012). Results from these studies carried out during the Science Demonstration Phase of the largest extragalactic surveys, the *Herschel* Multi-tiered Extragalactic Survey (HerMES; Oliver et al. 2012), the PACS Evolutionary Probe (PEP; Lutz et al. 2011) and the *Herschel* Astrophysical Terahertz Large Area Survey (H-ATLAS; Eales et al. 2010a), confirmed previous findings on the diversity of IR-luminous galaxy properties at high redshift, as well as the existence of high-redshift sources with no local equivalents, moving us closer in understanding the complex nature of the infrared galaxy population up to $z \sim 3$.

In this paper, we report a comprehensive study of the SEDs and dust temperatures of IR-luminous galaxies up to $z \sim 2$, using the deepest available *Herschel*/PACS and SPIRE data acquired as part of the PEP and HerMES consortia in the Cosmic Evolution Survey (COSMOS) and Great Observatories Origins Deep Survey [GOODS (N and S)] fields. A key aspect of our work is the attempt to eradicate survey selection effects, an issue which has plagued previous attempts to canvas the range of infrared SEDs (see Symeonidis et al. 2011a). Thus, for the first time we are able to examine the aggregate properties (infrared luminosity, dust temperature, SED shape) of IR galaxies within an almost entirely bias-free framework. The paper is laid out as follows: the introduction is followed by a section on the sample selection (Section 2) and SED measurements (Section 3). In Section 4 we discuss how we deal with AGN, in order to obtain a sample which is star formation dominated in the infrared. Section 5 is devoted to treatment of selection effects, enabling us to assemble a complete sample of IR galaxies. In Section 6 we present our results and discuss them in Section 7. Finally, our summary and conclusions are presented in Section 8. Throughout we employ a concordance ΛCDM cosmology of $H_0 = 70\ \mathrm{km\ s^{-1}\ Mpc^{-1}}$, $\Omega_\mathrm{M} = 1 - \Omega_\Lambda = 0.3$.

2 THE *HERSCHEL* SAMPLE

2.1 Initial selection

The starting point for this work is data from *Herschel*, covering three extragalactic fields: the GOODS-North and South (Giavalisco et al. 2004) and the COSMOS field (Scoville et al. 2007). We use PACS 100 and 160 μm and SPIRE 250, 350 and 500 μm images, acquired as part of PEP and HerMES, respectively. Source extraction from the PACS and SPIRE images[2] is performed on the *Spitzer*/IRAC 3.6 μm positions of the $f_{24} \geq 30$ μJy GOODS (N and S) sources and $f_{24} \geq 60$ μJy COSMOS sources, as described in Magnelli et al. (2009) and Roseboom et al. (2010, 2012). This method of source extraction on prior positions is widely used and enables the identification of secure counterparts over the whole SED. In this case however, its significant advantage lies in its ability to effectively deal with source blending in the *Herschel* bands, particularly for SPIRE where the beam is large (18.1, 24.9 and 36.6 arcsec full width at half-maximum at 250, 350 and 500 μm, respectively; Nguyen 2010). By using prior information to identify galaxies in the *Herschel* images, we are able to extract 'clean' photometry for each galaxy, even for those which appear blended in the PACS and SPIRE bands. For information on the GOODS *Spitzer*/MIPS 24 μm data see Magnelli et al. (2009), and for information on the COSMOS *Spitzer*/MIPS 24 μm data see Sanders et al. (2007) and Le Floc'h et al. (2009). The 3σ sensitivity limits of the PACS 100 and 160 μm catalogues, respectively, are

[1] *Herschel* is an ESA space observatory with science instruments provided by European-led Principal Investigator consortia and with important participation from NASA.

[2] The data presented in this paper will be released through the *Herschel* Database in Marseille HeDaM (hedam.oamp.fr/HerMES).

Table 1. The detection statistics of the *Herschel* sample used in this work. The first and second columns show the field and number of 24 μm sources with $f_{24} > 30$ and $f_{24} > 60$ μJy for GOODS (N and S) and COSMOS, respectively, whose positions are used as priors for source extraction in the *Herschel* bands. Column 3 shows the total number of 'isolated' 24 μm sources defined as having no companion within 8 arcsec; the percentage in parentheses is calculated out of the number in column 2. Column 4 shows the fraction detected at 100 and 160 μm, whereas column 5 shows the fraction detected at 160 and 250 μm. The final column shows what fraction of the 24 μm population is detected when the two criteria are used in disjunction, i.e. [100 and 160 μm] OR [160 and 250 μm]. This is the criterion used to select the initial *Herschel* sample (Section 2.1). The fractions shown in columns 4, 5 and 6 are out of the number of sources in column 3. As also mentioned in Section 2.1, the 3σ sensitivity limits of the PACS 100 and 160 μm catalogues, respectively, are 5 and 10 mJy for COSMOS, 3 and 6 mJy for GOODS-N and 1 and 2 mJy for GOODS-S. A 3σ detection in SPIRE using prior positions and the cross-identification method of Roseboom et al. (2010) is approximately 8, 11 and 13 mJy at 250, 350 and 500 μm in all fields.

Field	Number of 24μm sources	Number of 'isolated' 24 μm sources	Fraction detected at 100+160 μm (>3σ)	Fraction detected at 160+250 μm (>3σ)	Fraction detected at [100+160 μm] OR [160+250 μm]
(1)	(2)	(3)	(4)	(5)	(6)
GOODS-N	2149	1401 (65 per cent)	7 per cent	7 per cent	9 per cent
GOODS-S	2252	1580 (70 per cent)	21 per cent	9 per cent	22 per cent
COSMOS	52092	33 407 (64 per cent)	5 per cent	6 per cent	7 per cent

5 and 10 mJy for COSMOS, 3 and 6 mJy for GOODS-N and 1 and 2 mJy for GOODS-S. A 3σ detection in SPIRE using prior positions and the cross-identification method of Roseboom et al. (2010) is approximately 8, 11 and 13 mJy at 250, 350 and 500 μm in all fields. In the case of the PACS bands, σ is only the photometric error, whereas for the SPIRE bands, σ includes confusion error (see Nguyen 2010 for the SPIRE confusion limits).

The initial selection for our sample includes all 24 μm sources that have detections (at least 3σ) at [100 and 160 μm] OR [160 and 250 μm] (where 'OR' is the operator representing disjunction in Boolean logic; i.e. it returns 'true' if either or both conditions are satisfied). This ensures that (i) the sample consists of IR-luminous galaxies ($L_{\rm IR} > 10^{10}$ L$_\odot$), (ii) the sample is as complete as possible over a large redshift range with respect to SED types, given the PACS and SPIRE selection functions (see Section 5 for more details) and (iii) there are at least three reliable photometric points in the SED (24 μm+ two *Herschel* bands) for subsequent measurements.

Our selection is in essence a colour selection rather than a single band selection, as we require sources to be detected at both 24 and 160 μm (the additional *Herschel* photometry at 100 or 250 μm has a small effect on the sample selection but enables more accurate SED measurements; see Section 5). As a result, the detection rate is more strongly dependent on the SED shape, in our case the mid-to-far-IR continuum slope, than for a typical flux limited survey. Given the flux limits reported earlier, the 24 μm survey is 66, 166 and 200 times deeper than the PACS 160 μm survey in GOODS-S, COSMOS and GOODS-N, respectively. We find that the different ratios in flux density limits ($f_{160}^{\rm lim}/f_{24}^{\rm lim}$) between the three fields introduce a bias with respect to the SED shapes that are detected in each survey particularly for objects with flux densities close to the limit. To mitigate this effect, we match the relative PACS 24 μm depths of the GOODS fields to the COSMOS survey, as the latter covers the largest area and hence dominates the statistics of the final sample. This is done as follows: the GOODS-S sample is cut at $f_{160} = 5$ mJy and the GOODS-N sample is cut at $f_{24} = 36$ μJy, so that $f_{160}^{\rm lim}/f_{24}^{\rm lim} \sim 166$ in all cases. Note that matching the samples in this way ensures that the *relative* biases between the surveys are minimized, i.e. that all three surveys probe the same range of SED types. However, it does not deal with *absolute* biases; these are dealt with in Section 5.

Besides the photometric selection criteria, we also restrict the sample to sources which have no other 24 μm companions within 8 arcsec, i.e. 'isolated' sources. This allows us to work with more reliable photometry, as at the longer wavelengths, where the *Herschel* beam is large, flux extraction in the *Herschel* bands can be problematic when dealing with blended sources. The choice of an 8 arcsec radius is larger than the 24 μm beam (6 arcsec) and visual inspection shows that it is sufficient to eliminate problematic blends. In addition, 8 arcsec is the scale of the first airy ring of bright 24 μm sources. In the cases where there is a companion within the first airy ring, the *Herschel* flux is assigned to the bright source in the centre, if the companion source is 10 or more times fainter (Roseboom et al. 2010). By eliminating such cases from our sample, we avoid the occurrence of a potential bias causing the measured *Herschel* flux density to positively correlate with the 24 μm flux density. As a result, for the 24 μm sources we subsequently use, there have been no prior assumptions when assigning *Herschel* fluxes. This is confirmed by performing a Kolmogorov–Smirnov (K-S) test on the flux density distribution of the whole 24 μm population and that of the 'isolated' 24 μm sources in each field. We find the two to be entirely consistent, suggesting that our approach works well

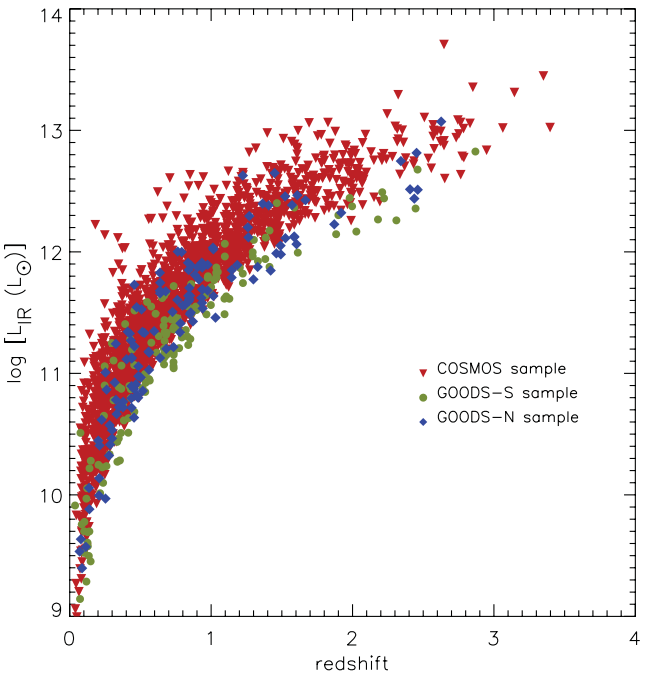

Figure 1. Total infrared luminosity as a function of redshift for the initial *Herschel* sample of 2313 sources used for SED measurements (Section 3).

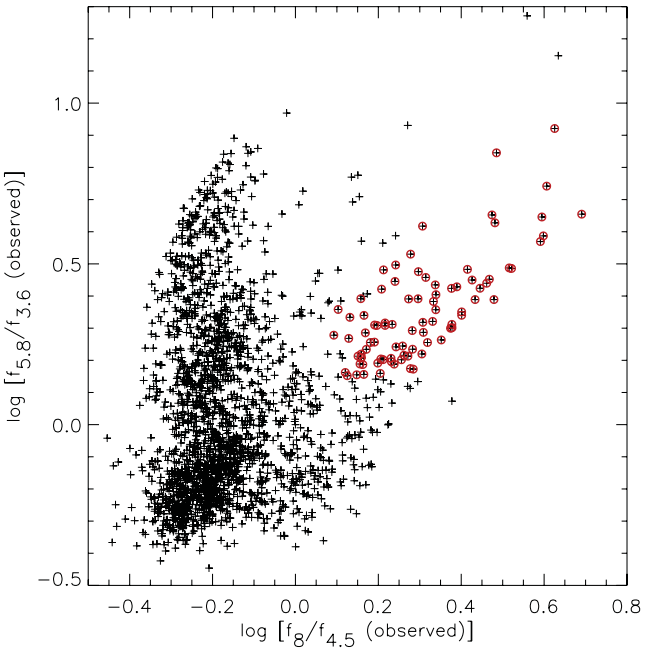

Figure 2. Observed *Spitzer*/IRAC colours ($f_{5.8}/f_{3.6}$ versus $f_8/f_{4.5}$) for the *Herschel* sample (black crosses). The red circles denote sources which are identified as AGN dominated in the near/mid-IR using the IRAC criteria outlined in Donley et al. (2012).

in eliminating potentially problematic sources without introducing systematic biases.

At this point, our assembled *Herschel* sample consists of 2500 sources (2206 from COSMOS, 173 from GOODS-S and 121 from GOODS-N). Some statistics for the initial sample are shown in Table 1.

2.2 Redshifts

The redshifts we use are a combination of spectroscopic and photometric, assembled from various catalogues: Berta et al. (2011) for GOODS-N, Cardamone et al. (2010) and Santini et al. (2009) for GOODS-S and Ilbert et al. (2009) and Salvato et al. (2009, 2011) for COSMOS. The optical positions of sources in these catalogues are cross-matched to the 24 μm positions within 1 arcsec. The excellent photometric coverage of these fields and high-quality photometric redshifts available result in >90 per cent of the sources in our sample having a usable redshift (25 per cent spectroscopic; although for the final sample about 1/3 are spectroscopic), leaving 2313 *Herschel* sources for subsequent analysis. For more details on the quality of photometric redshifts see Appendix A, where we also show that the use of photometric redshifts does not bias our results.

3 MEASUREMENTS

We fit the photometry of the *Herschel* sample, with the Siebenmorgen & Krügel (2007, hereafter SK07) library of 7208 models, built on the formulation of Krügel & Siebenmorgen (1994). This library of templates ranges in five free parameters, in physically acceptable combinations, and the shape of each template is determined by the combination of parameters which define it:

(i) the radius of the IR emitting starburst region (R), taking discrete values of 0.35, 1, 3, 9, 15 kpc,

(ii) the total luminosity of the system ($L_{\rm tot}$) ranging from 10^{10} to 10^{15} $L_\odot$,

(iii) the visual extinction from the edge to the centre of the starburst, taking discrete values of 2.2, 4.5, 7, 9, 18, 35, 70 and 120 mag,

(iv) the ratio of the luminosity of OB stars with hot spots to the total luminosity ($L_{\rm OB}/L_{\rm tot}$) taking discrete values of 40, 60 and 90 per cent for the ≤3 kpc models and 100 per cent for the 9 and 15 kpc models and

(v) the dust density in the hot spots in units of hydrogen number density (cm^{-3}) ranging from 100 to 10 000, in discrete steps.

As mentioned earlier, six-band photometry is available – 24 μm from *Spitzer*/MIPS, 100, 160 from *Herschel*/ PACS and 250, 350, 500μm from *Herschel*/SPIRE – and at least three bands, always including the 24 and 160 μm data, are used in the fitting. The normalization of the templates is varied in order to minimize χ^2. The 0.68 lower and upper confidence limits for our computed parameters resulting from the fits (e.g. total infrared luminosity, etc.) are calculated according to the prescribed χ^2 confidence intervals for one interesting parameter, namely $\chi^2_{\rm min}+1$, where $\chi^2_{\rm min}$ is the minimum χ^2.

Note that because our photometry only sparsely samples the full IR SED, the parameters that characterize the best-fitting SEDs within $\chi^2_{\rm min}+1$ are often degenerate and not well constrained. In addition, each object in the sample is fitted with the entire SK07 library irrespective of the inherent luminosity of the templates; the total infrared luminosity, $L_{\rm IR}$ ($L_\odot$), of each source is computed by integrating the best matched SED model between 8 and 1000 μm (see Fig. 1 for a plot of $L_{\rm IR}$ as a function of redshift). This allows us to stay clear of any assumptions which link the SED shape to the luminosity. However, it also implies that we cannot directly use some of the SK07 parameters to describe our sample, as they require scaling. One such parameter is the starburst size, as its impact on the SED shape depends on the total input luminosity. Finally, the SK07 grid, although more flexible than most stand-alone SED libraries currently in the public domain, is still too coarse to allow complete characterization of the physical properties of the sample. For these reasons, we opt to use one parameter to describe the overall shape of the SK07 SED templates; we refer to this as the flux ($\mathcal{F}$), calculated as $\log[L_{\rm tot}/4\pi R^2]$ in units of $L_\odot$ kpc^{-2}, where $L_{\rm tot}$ is the given luminosity of the template (not our computed $L_{\rm IR}$) and R is the starburst size that corresponds to that template. In the SK07 formulation, for constant A_V, as R becomes larger, the dust mass increases as a function of R^2 and hence becomes cooler, with the temperature being a function of $L_{\rm tot}/R^2$. Hence, the larger the $\mathcal{F}$, the more the flux reaches the edge of the starburst region and therefore the dust emission is warmer. One can interpret high and low values of $\mathcal{F}$ as representative of systems with warmer/more compact and cooler/more extended dust emission, respectively.

In order to calculate dust temperatures, we use a modified blackbody function (a grey-body), of the form $B_\lambda(T)(1-{\rm e}^{-\tau_\lambda})$, with a wavelength-dependent optical depth $\tau_\lambda=\tau_{100\,\mu{\rm m}}(100\,\mu{\rm m}/\lambda)^\beta$ (e.g. see Klaas et al. 2001) and a dust emissivity index β. We assume a low opacity limit, so approximate the term $(1-{\rm e}^{-\tau_\lambda})$ by $\lambda^{-\beta}$. Typical reported values of β range between 1.5 and 2 (e.g. Dunne et al. 2000; Lisenfeld et al. 2000) and we adopt $\beta=1.5$, consistent with studies of the far-IR emissivity of large grains (Desert, Boulanger & Puget 1990). The temperatures are derived by fitting all photometry at $\lambda\geq\lambda_{i_{\rm max}-1}$, where i denotes a *Herschel* band (100, 160, 250, 350, 500 μm) and $i_{\rm max}$ is the band which corresponds to the maximum

flux (νf_ν); the 24 μm photometry is never included in the fitting. Note that although some studies have shown that a two-temperature grey-body model (e.g. Dunne & Eales 2001; Klaas et al. 2001) is a more accurate description of far-IR dust-emission, this would not work with our available photometry; much longer wavelength data would be needed especially for sources at high redshift. However, in any case, our aim is to measure the average dust temperature of the far-IR peak for each source; thus, a single temperature grey-body model is required. Our method gives a temperature which is most representative of the peak dust emission.

4 DEALING WITH AGN CONTAMINATION

As this work targets the properties of the star-forming galaxy population, objects whose infrared energy budget potentially includes a significant contribution from an AGN need to be removed from the sample. Although the fraction of *Herschel* galaxies found to host AGN is high (up to 30 per cent; Symeonidis et al. 2011b), it has been shown that AGN in far-IR-selected galaxies do not often dominate the infrared or total energy budget of the system. According to an energy balance argument, if the AGN is energetic enough to contribute significantly to the infrared emission of a starburst galaxy, then its signature is likely to emerge in the mid-IR part of the SED in the form of a power-law continuum (e.g. Symeonidis et al. 2010). As a result, the most suitable way to identify such objects is examining their colours in the *Spitzer*/IRAC (3.6, 4.5, 5.8, 8 μm) bands. Until recently, the most commonly used IRAC AGN selection criteria have been those presented in Lacy et al. (2004) and Stern et al. (2005). However, as shown in Yun et al. (2008) and Donley et al. (2012), there is a non-negligible chance that IR/submm selected galaxies will be erroneously identified as AGN dominated in the IRAC bands. In addition, Hatziminaoglou, Fritz & Jarrett (2009) reported 'cross-talk' between the AGN and starburst loci in the Lacy et al. (2004) diagram. Here, we use the Donley et al. (2012) IRAC criteria, shown to be effective in picking out AGN and sufficiently robust against misidentifications. Fig. 2 shows the $f_{5.8}/f_{3.6}$ colour against the $f_8/f_{4.5}$ colour for the *Herschel* sample. Indicated in red are the sources which satisfy the Donley et al. (2012) criteria and are hence classified as AGN dominated in the near/mid-IR. These 87 (out of 2313) objects, ∼4 per cent, are subsequently excluded from the sample, leaving 2226 sources. Note that this is not the fraction of AGN hosted by *Herschel* sources, rather it is the fraction of objects where the AGN could contribute substantially in the mid-infrared and hence interfere with our analysis. A 4 per cent fraction of sources with AGN-dominated near/mid-IR SEDs is in line with results from Symeonidis et al. (2010) and Pozzi et al. (2012) who show that typical AGN rarely contribute more than 20 per cent in the IR emission of far-IR selected systems (see also Hatziminaoglou et al. 2010; Page et al. 2012; Nordon et al. 2012; Rosario et al. 2012).

5 DEALING WITH SELECTION EFFECTS

5.1 *Herschel* selection

To accurately characterize the aggregate properties of the IR-luminous population and their evolution with redshift, there should be no bias with regard to the SED types we can observe, particularly regarding the far-IR where all our measurements are performed. As a result, the accuracy of our work rests on minimizing selection biases and assembling a sample within an unbiased part of the $L-z$ parameter space. For this purpose, we use the method described in Symeonidis et al. (2011a) to examine the selection functions of the PACS and SPIRE bands, mapping out an SED–redshift–luminosity parameter space at the flux density limits of the GOODS and COSMOS surveys used in this work.

Fig. 3 shows the $L_{\rm IR}$ ∼10^{11} and 10^{12} $L_\odot$ selection functions for MIPS 24 μm, PACS 100, 160 μm and SPIRE 250, 350 and 500 μm at the COSMOS flux density limits. As also explained in detail in Symeonidis et al. (2011a), Fig. 3 is created by using all SED templates from the SK07 library, normalizing them to the required total IR luminosity and then scaling and redshifting them to the observed frame. Each SED template is then convolved with the MIPS, PACS and SPIRE filter transmission curves in order to compute the weighted integrated flux within each filter. We subsequently perform a colour correction (according to the prescription in the instruments' observer manuals) in order to obtain a monochromatic flux density in each band, derived with the same spectral shape used to calculate the measured flux density of real sources. For each band, we then compare our template monochromatic flux density to the flux density limit in order to determine whether an object with the given redshift, luminosity and SED shape would be part of our sample. This results in the selection functions presented in Fig. 3. The red thick patterns mark the regions where all templates of a given peak wavelength are detected, whereas the blue and green dashed patterns indicate regions where only 90 and 70 per cent of the SK07 templates are recovered, respectively. The detection rate relates to variations in SED shape; for example, for the MIPS 24 μm selection function, only luminous SEDs with strong PAH features will be detected at $z \sim 1.7$. In the unshaded areas less than 70 per cent of templates are detectable, a fraction which reduces to zero above a certain redshift.

Note that the selection functions of PACS and SPIRE overlap significantly, suggesting that the SEDs of most sources will be fully sampled by the *Herschel* photometry. However, there are large differences between the MIPS/24 μm and the *Herschel* selection functions, especially at 500 μm. This is not surprising as they probe different parts of the SED and it is expected that the long-wavelength one eventually turns to favour very cold sources and the short-wavelength one eventually turns to favour warm sources. The 24 μm selection is a steep function of SED shape: SEDs with a significant warm dust component are favoured up to very high redshifts. The small area covered by the red pattern implies that it is only over a small redshift range that all SED shapes are recoverable. However, the large blue and green shaded regions indicate that cold SEDs *can* be detected up to high redshift, as long as they do not have a high far-IR-to-mid-IR ratio.

Ignoring the 24 μm selection for the moment, Fig. 3 shows that our far-IR selection criteria of a detection at [100+160 μm] OR [160+250 μm] will result in the largest number of sources detected in an unbiased part of L–z space. This is more clear in Fig. 4 which shows the [100+160μm] selection function (top panel), the [160+250 μm] selection function (middle panel) and the two criteria in disjunction[3] ([100+160 μm] OR [160+250 μm]; lower panel) for $\log(L_{\rm IR}/L_\odot) = 11.5$, at the COSMOS limits. The black boxes outline the extent in redshift whereby all SEDs with peak between 50 and 140 μm will be detected. This translates to a temperature range of 18–52 K, using the Wien displacement law for a νf_ν grey body, $T(K) \sim \frac{hc}{(4+\beta)k\lambda_{\rm peak}}$, where h is the Planck constant, c is the speed of light in a vacuum and k is the Boltzmann constant

[3] We remind the reader, that, as also mentioned in section 2.1, disjunction in Boolean logic returns 'true' if either or both conditions are satisfied.

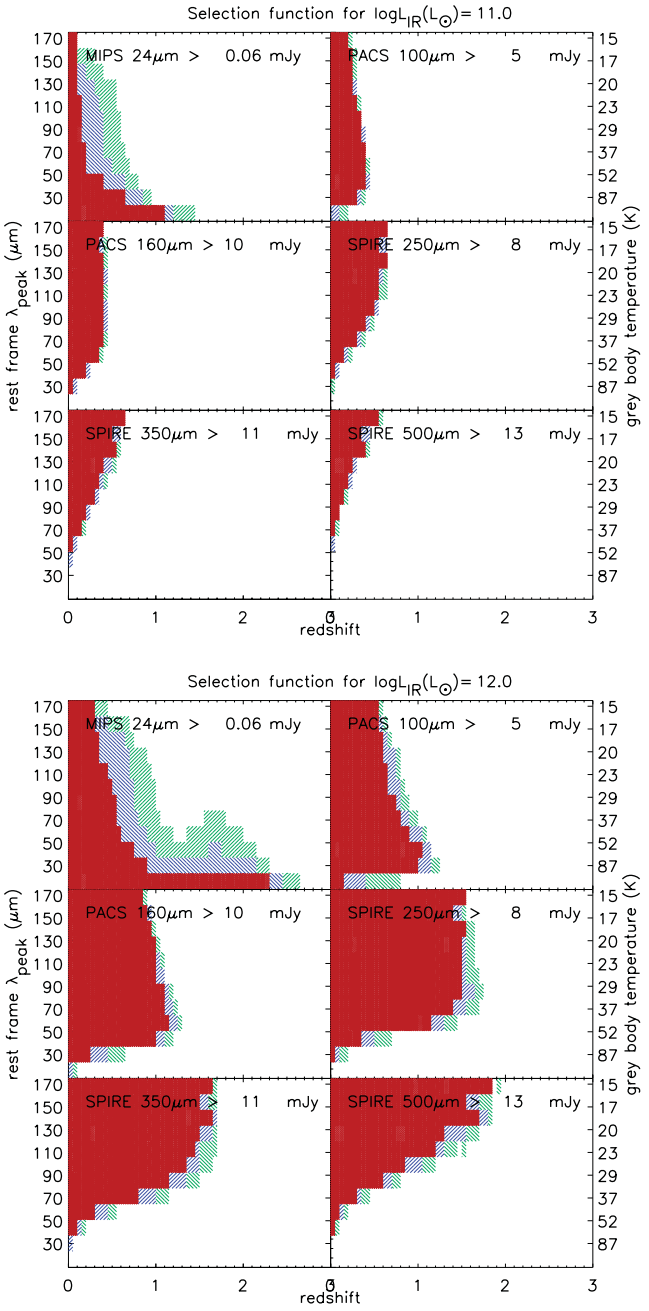

Figure 3. $\log(L_{\rm IR}/{\rm L}_\odot) = 11$ and $\log(L_{\rm IR}/{\rm L}_\odot) = 12$ selection functions for PACS and SPIRE, constructed using the SK07 model library; see also Symeonidis et al. (2011a). The plot shows SED peak wavelength (left *y*-axis) and grey-body temperature (right *y*-axis) as a function of redshift. At any redshift slice and for a given flux density limit, the red region indicates that all SED shapes of the corresponding peak wavelength are detectable, whereas the blue and green dashed patterns indicate regions where only 90 and 70 per cent of the SK07 templates are recovered, respectively. In the unshaded areas less than 70 per cent of templates are detectable, reaching zero above a certain redshift. The flux density limits used to construct these diagrams are 0.06, 5, 10, 8, 11 and 13 mJy for the 24, 100, 160, 250, 350 and 500 μm bands, respectively, corresponding to the COSMOS 3σ flux density limits.

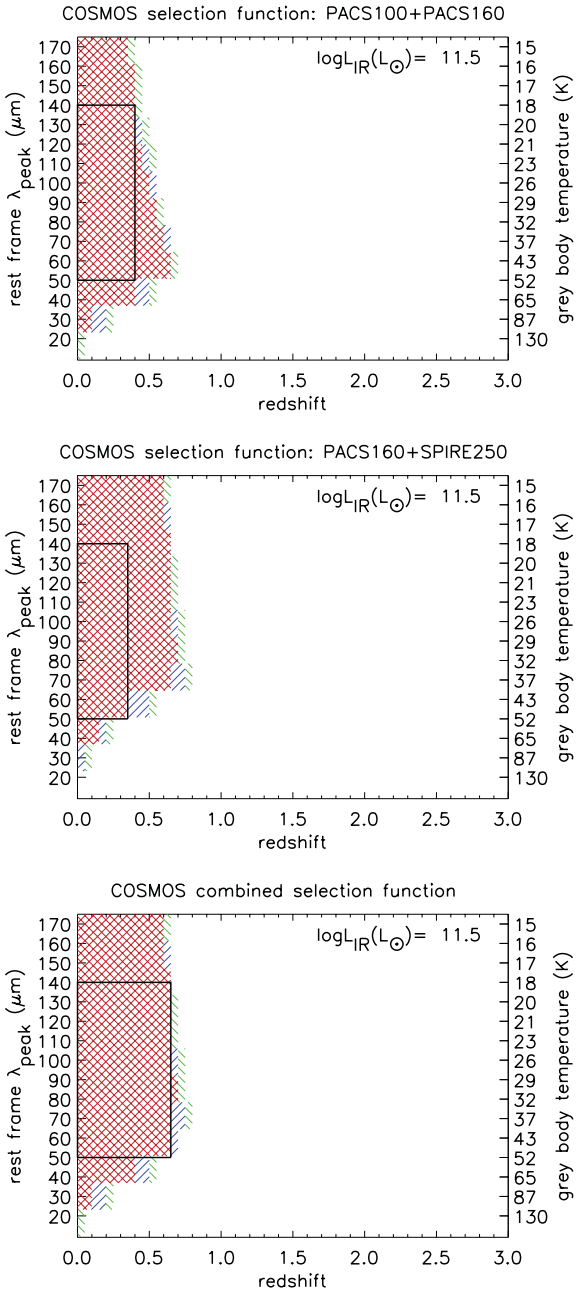

Figure 4. Selection functions for $\log(L_{\rm IR}/{\rm L}_\odot) = 11.5$ using the PACS 100+160 μm criterion (top panel), the PACS 160 + SPIRE 250 μm criterion (middle panel) and the two used in disjunction ([100+160 μm] OR [160+250 μm]). The plot shows SED peak wavelength (left *y*-axis) and grey-body temperature (right *y*-axis) as a function of redshift. At any redshift slice and for a given flux density limit, the red region indicates that all SED shapes of the corresponding peak wavelength are detectable, whereas the blue and green dashed patterns indicate regions where only 90 and 70 per cent of the SK07 templates are recovered, respectively. In the unshaded areas less than 70 per cent of templates are detectable, reaching zero above a certain redshift. The flux density limits used to construct these diagrams are 5, 10 and 8 mJy for the 100, 160 and 250 μm bands, respectively, corresponding to the 3σ flux density limits in COSMOS. The black box in each panel outlines the redshift range where all SED shapes with peak wavelengths 50–140 μm are detectable – note that the redshift range is larger in the third panel.

and we take the dust emissivity (β) to be 1.5. This choice of peak wavelength/temperature range is the best compromise between the range of SED types probed and the number of objects studied. As we shall see in Section 6, increasing that range would not have changed the measured average properties of the sample but would have significantly reduced the statistics. The black box in the lower panel of Fig. 4 shows that using the two criteria in disjunction, i.e. [100+160 μm] OR [160+250 μm], allows $\log(L_{\rm IR}/{\rm L}_{\odot}) = 11.5$ sources to be selected up to much higher redshifts, than when these criteria are used separately.

With the aid of the combined selection functions, we now define the complete $L_{\rm IR}$–z parameter space for each survey (GOODS-N, GOODS-S and COSMOS), shown in Fig. 5, where the curves separate the complete (below curve) and incomplete (above curve) part of the parameter space. The space below the curves indicates the $L_{\rm IR}$–z range, where any source with SED peak wavelength within $50 < \lambda_{\rm peak}(\mu{\rm m}) < 140$, or, equivalently, temperature within $18 \lesssim T({\rm K}) \lesssim 52$, is detectable. As mentioned earlier, the [100+160 μm] criterion (green curve in Fig. 5) picks up more sources at low redshift but excludes more high-redshift sources because its selection function quickly turns over to favour warm SEDs providing a limited unbiased L–z space at high redshift. On the other hand, the [160+250 μm] criterion (blue curve in Fig. 5) performs poorly at low redshift, because the SPIRE 250 μm which mainly drives the combined selection function largely favours cold sources. At $z \sim 1$, the combination of 160 and 250 μm turns over as now these bands are sampling 80 and 125μm, respectively, covering the bulk of IR emission. The combined criterion of [100+160 μm] OR [160+250 μm] (red curve in Fig. 5) is what we thus use to select the final sample used in this work. Note that it is the 160 μm band that principally drives the combined selection function, whereas the PACS 100 μm and SPIRE 250 μm in essence provide an additional band in the infrared, vital for our analysis. However, as they complement each other well, such that most SEDs missed at 100 μm are picked up at 250 μm and vice versa, the complete region below the red curve in Fig. 5 includes many sources which are in the incompleteness regions of both the blue and green curves. In addition, this selection criterion ensures that the SED peak is well sampled for most sources up to $z \sim 2$.

Although the selection outlined above is quite conservative since it is unlikely that all SK07 models with $50 < \lambda_{\rm peak}(\mu{\rm m}) < 140$ are representative of real objects, it nevertheless allows us to perform our analysis within a bias-free framework with respect to the PACS and SPIRE surveys. Hereafter, our study concerns only the 1159 sources within the complete parameter space below the red curves in Fig. 5. The redshift distribution of the final *Herschel* sample is shown in Fig. 6.

5.2 The 24 μm selection

In Section 5.1 we assembled a complete sample with respect to the *Herschel* bands, which cover the part of the SED primarily used in our study (see Section 6). It is now important to examine whether the requirement for a 24 μm detection affects the completeness of this sample.

Fig. 3 shows that although the 24 and 160 μm selection functions cover approximately the same redshift range, some SEDs are systematically missed at 24 μm. We investigate this further by aiming to answer the following questions: what types of SEDs are missed, how common are sources with such SED types and how does this affect our results? The first question is easier to answer. These SEDs are ones with high far-to-mid-IR ratio, resulting from a combination

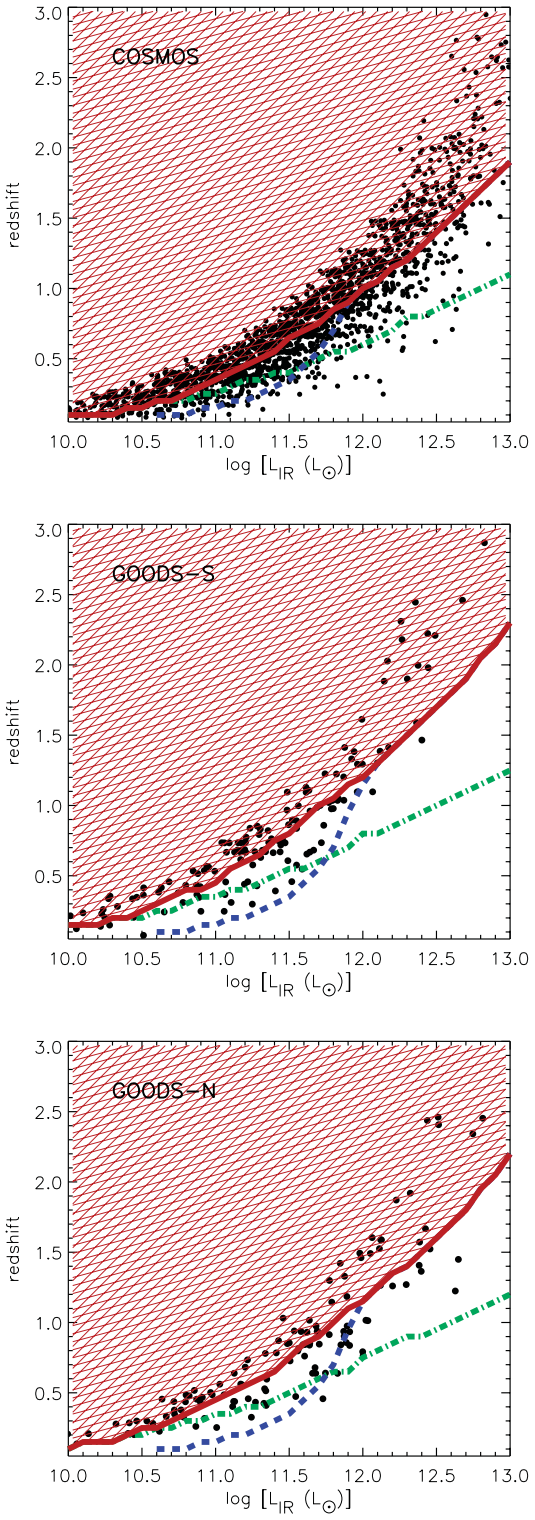

Figure 5. Redshift versus $L_{\rm IR}$ for the *Herschel* sources (black points) in COSMOS, GOODS-S and GOODS-N. The regions below the green and blue dashed lines mark the complete parameter space derived from the [100+160 μm] and [160+250 μm] selection functions, respectively. The red curve corresponds to the parameter space traced out by the two criteria in disjunction ([100+160 μm] OR [160+250 μm]), with the hatched red pattern indicating the region of incompleteness. In the work presented in this paper we use only sources which lie below the red curve, which includes any source with $50 < \lambda_{\rm peak}(\mu{\rm m}) < 140$, or, equivalently, temperature within $18 \lesssim T({\rm K}) \lesssim 52$.

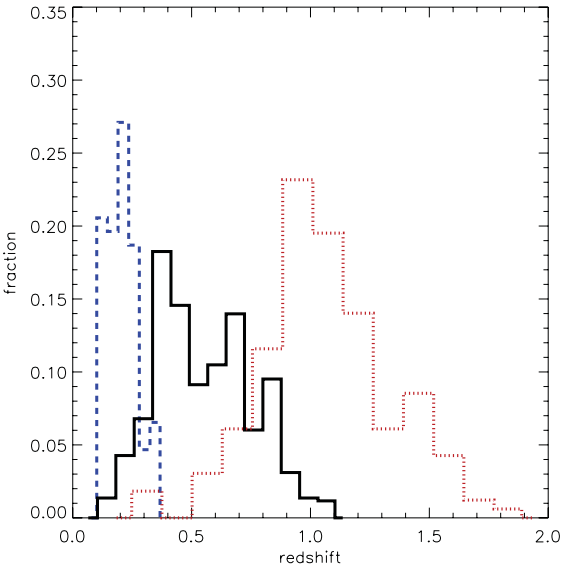

Figure 6. The redshift distribution of the final *Herschel* sample of 1159 sources used in this work; the dashed blue line for normal IR galaxies (NIRGs), the solid black line for LIRGs and the red dotted line for ULIRGs.

of parameters in the SK07 formulation, such as high extinction ($A_V > 70$) and/or low luminosity and/or low dust density within the hotspot, with a detection rate that is also redshift dependent. Examples of these SEDs (in the observed frame) are presented in Fig. 7, and Fig. 8 shows the f_{500}/f_{160}–f_{160}/f_{24} colour space these cover; in both figures we assume the COSMOS flux limits. Fig. 7 shows that such templates are characterized by steep mid-IR continua and strong silicate absorption features at 9.7 and 18 μm, a result of high extinction in the SK07 formulation. Note that these SED types are easily detected in the *Herschel* bands. In both panels of Fig. 8, we also show the SED of Arp 220 (taken from SK07), normalized at the appropriate luminosity and redshift. Arp 220 is one of the most optically thick ULIRGs known (e.g. Papadopoulos, Isaak & van der Werf 2010), so it is interesting to examine whether it would be detected in our sample. The top panel shows that at low redshift it would be detected in all bands; however, at $z = 0.9$ it is only just detected at 24 μm, but easily detected with *Herschel*. As this SED is redshifted further, it will be missed by the 24 μm survey, suggesting that optically thick SEDs, with deep silicate absorption, would not be in our sample at high redshift ($z \gtrsim 1$).

Fig. 8 shows the observed f_{500}/f_{160} versus f_{160}/f_{24} colours for the COSMOS sample as well as for sources in the GOODS samples which fall within the COSMOS completeness region shown in Fig. 5. The grey shaded region is the parameter space occupied by the SED templates which are detected in the *Herschel* bands within the complete L_{IR}–z parameter space for COSMOS outlined in Fig. 5, but are missed by the 24 μm selection. Some overlap between the samples and shaded region should be expected, as some sources could have high f_{160}/f_{24} ratios because of high f_{160} rather than a low f_{24}. However, we see very little overlap, suggesting that the detected and non-detected SEDs cover a significantly different part of parameter space in terms of their far-to-mid-IR colour. This implies that, on average, SEDs are missed by the 24 μm selection because of a particular feature that reduces the amount of 24 μm observed flux, such as a silicate feature, rather than an inherently steep far-to-mid-IR continuum. This also becomes obvious from the values of f_{160}/f_{24} ratios that some templates have: such high values of f_{160}/f_{24}, up to six orders of magnitude, can only be caused by

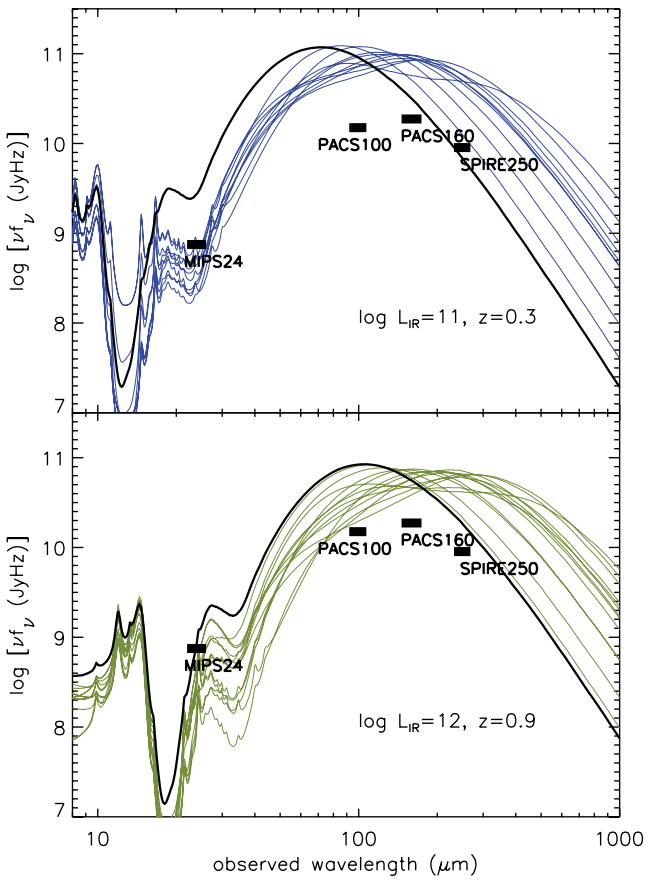

Figure 7. Example SED templates from the SK07 library, shown in the observed frame. In the top panel they are normalized to a luminosity of $L_{IR} = 10^{11}$ $L_\odot$ and then scaled and redshifted to $z = 0.3$. In the lower panel they are normalized to a luminosity of $L_{IR} = 10^{12}$ $L_\odot$ and scaled and redshifted to $z = 0.9$. At these luminosities and redshifts, these templates would not be detected down to the 60 μJy COSMOS 24 μm flux density limit. However, they are detected in the *Herschel* bands at the COSMOS 3σ 100, 160, 250 μm limits, also shown in both panels. For comparison, the SED of Arp 220 (black SED; taken from SK07) is also plotted normalized at the appropriate luminosity and redshifted. Note that at $z = 0.9$, it is only just detected.

a strong 9.7 μm silicate feature; c.f. with what is observed for the Arp 220 SED redshifted at $z = 1.5$, where the 9.7 μm feature falls in the 24 μm band. In terms of the f_{500}/f_{160} ratio, there are only a handful of *Herschel* sources with $f_{500}/f_{160} > 1$, whereas a significant fraction of the templates in the grey region have such cold colours. This is not surprising as we would expect some of the templates that are missed at 24 μm to be overall colder and hence have higher f_{500}/f_{160}; see some examples in Fig. 7.

To answer the second question 'how common are these SED types?', we compare the GOODS (N and S) to the COSMOS colours in Fig. 8. As mentioned earlier, the GOODS sources shown in Fig. 8 are within the COSMOS completeness region mapped out in Fig. 5. However, for GOODS, the 24 μm flux density limit is twice as deep as it is in COSMOS, so in principle these GOODS sources could have SEDs with $f_{160}/f_{24} > 330$. We do not find any such sources; in fact, we note that GOODS objects have f_{160}/f_{24} ratios within the range covered by COSMOS, suggesting that SEDs with high f_{160}/f_{24} (up to $z \sim 2$) are rare.

In Fig. 9 we examine the flux density distribution of the 24 μm population in the three fields under study, in comparison to the

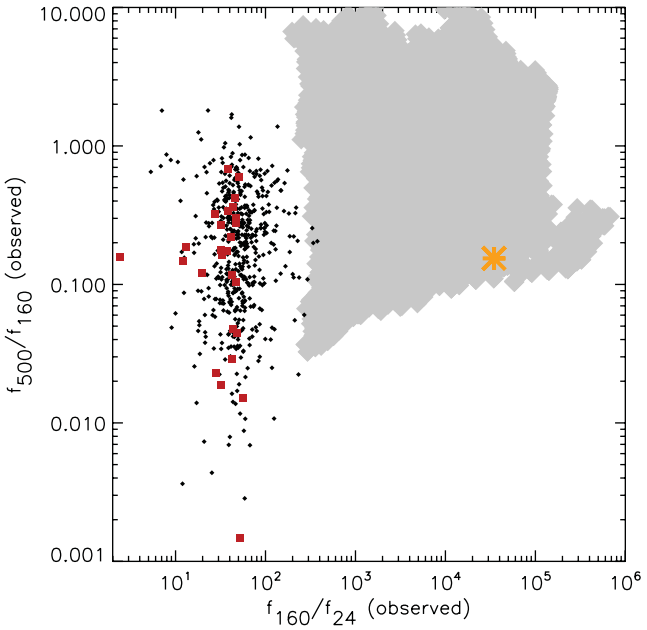

Figure 8. Observed f_{500}/f_{160} versus f_{160}/f_{24} colour. The grey shaded region shows the colours of SK07 templates, detected in the *Herschel* bands within the complete COSMOS $L-z$ parameter space outlined in Fig. 5, but missed by the COSMOS 24 μm selection (some examples of these templates are shown in Fig. 7). The small black diamonds denote the COSMOS sample and red squares denote the GOODS-S and GOODS-N sources within the COSMOS $L-z$ completeness region (Fig. 5). The orange asterisk shows the colours for the SK07 SED of Arp 220 redshifted to $z = 1.5$.

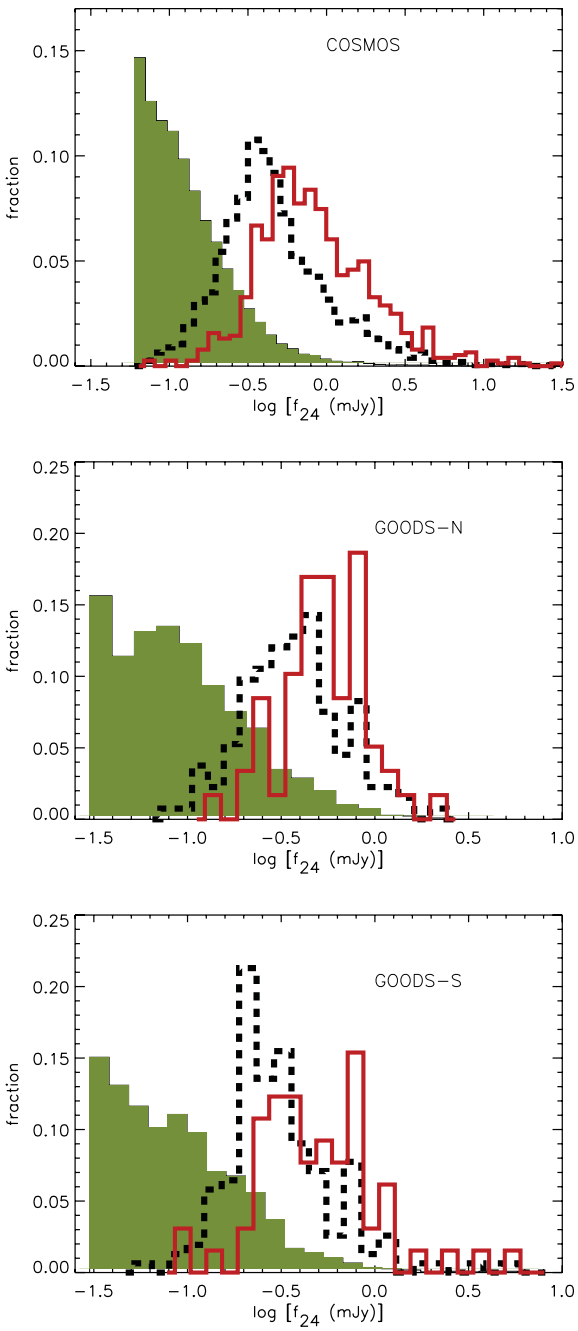

Figure 9. The 24 μm flux density distribution of the 24 μm population in COSMOS, GOODS-N and GOODS-S (green filled-in histogram) compared to that of the final *Herschel* sample before (black dashed histogram) and after the *Herschel* completeness criteria are applied (red solid histogram; see Section 5.1).

distribution of *Herschel* sources before and after the *Herschel* completeness criteria are applied (Section 5.1). Note the significant offset between the distributions of *Herschel* sources and that of the 24 μm population, suggesting that *Herschel* flux densities are intrinsically correlated with bright 24 μm flux densities. This is unlikely to be an artefact of our selection, as we are using only 'isolated' 24 μm objects, so there is no reason why, in principle, a *Herschel* source cannot be associated with a faint 24 μm source. It is immediately obvious from Fig. 9 that the fraction of sources which would not be part of our sample because of the requirement of a 24 μm detection is very small. Assuming normally distributed flux densities and by calculating the mean and standard deviation of each distribution, we can compute $n\sigma$ where n is the number of standard deviations (σ), at the location of the 24 μm flux density limit. This gives a rough indication of the fraction of sources that are likely missed due to the 24 μm selection. Before the *Herschel* completeness criteria are applied, we estimate that 0.1, 1.4 and 0.01 per cent of sources are unaccounted for in GOODS-S, COSMOS and GOODS-N, respectively. After these criteria are applied, the fraction of missing sources in COSMOS goes down to 0.2 per cent, whereas for the GOODS fields it is less than 0.06 per cent. Although these are rough estimates and rest on the assumption of normally distributed flux densities, they do indicate that the fraction of sources missed by the 24 μm selection is very small once our final sample is assembled in the complete $L-z$ parameter space using the *Herschel* selection functions (Section 5.1).

In light of this analysis, we conclude that (i) the SEDs missed by the 24 μm selection have high far-to-mid-IR ratios, mainly as a result of high optical depth in the mid-IR and deep silicate features, (ii) these SEDs are not a common occurrence amongst IR-luminous galaxies up to $z \sim 2$ and (iii) our final *Herschel* sample can be assumed to be complete in terms of the SED types we can detect. Our findings are consistent with the study of Magdis et al. (2011) who found the *Herschel* 24 μm dropouts to constitute a few per cent of the IR-luminous galaxy population at high redshift and concluded that they must be sources with stronger silicate absorption features – see also Roseboom et al. (2010) and Lutz et al. (2011) for discussion of 24 μm selection effects. Finally the third question of 'how would the fraction of sources missed affect our results?' is discussed at the end of Section 6.4.

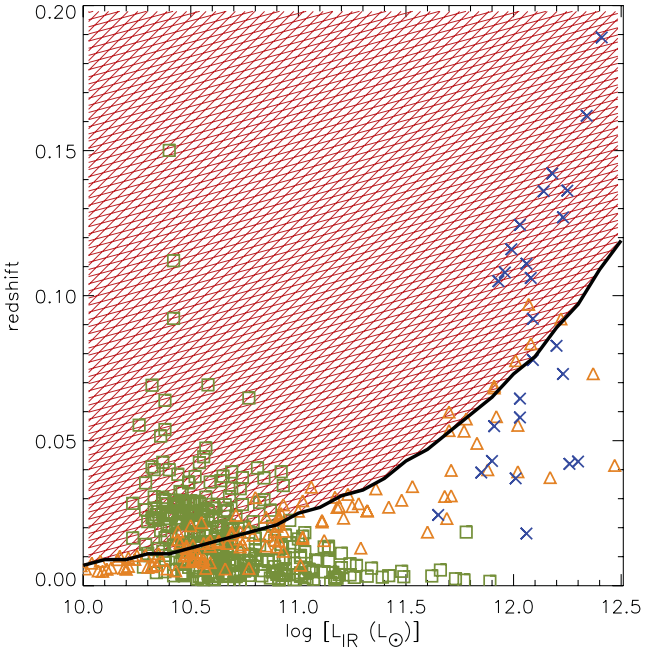

Figure 10. Plot of redshift versus total infrared luminosity for the local ($z \lesssim 0.1$) samples (see Section 5.3); blue crosses: Clements et al. (2010), orange triangles: Hwang et al. (2010) and green squares: Buat et al. (2010). The region below the black curve marks the complete parameter space corresponding to the *IRAS* 1 Jy 60 μm selection function, with the hatched red pattern indicating the region of incompleteness. Only sources below the curve are used in our analysis.

5.3 Local sample selection

In order to compare the *Herschel* sample to analogous sources in the nearby ($z \lesssim 0.1$) Universe, we also assemble an *IRAS*-selected local sample of $L_{\rm IR} > 10^{10}$ L$_\odot$ galaxies by combining sources from Clements et al. (2010), Hwang et al. (2010) and Buat et al. (2010). For the Clements et al. (2010) objects, we retrieve their published single grey-body temperatures and total infrared luminosities calculated using *IRAS* 60 and 100 μm data as well as SCUBA data. For the other two samples (Hwang et al. 2010 and Buat et al. 2010), we use their computed total infrared luminosities and calculate grey-body temperatures by fitting a grey-body function of emissivity $\beta = 1.5$ (see Section 3) to the *IRAS* and *AKARI* fluxes at $\lambda \geq 60$ μm. In all cases, the SEDs of the local sources have some coverage at ≥100 μm, either because of *AKARI* or SCUBA data.

In order to combine these samples for subsequent analysis, we select all sources which are in the complete $L-z$ region of the *IRAS*/60 μm selection function down to a flux density of 1 Jy [see the method in Section 5 and Symeonidis et al. (2011a) for the *IRAS* selection function]. Fig. 10 shows the curve dividing complete and incomplete parts of parameter space. We cut the local samples to include only sources in the complete parameter space, where any source with $f_{60} > 1$ Jy and SED peak wavelength within $50 < \lambda_{\rm peak}(\mu{\rm m}) < 140$, or, equivalently, temperature within $18 \lesssim T({\rm K}) \lesssim 52$, is detectable.

6 RESULTS

6.1 SED characteristics

Typical SEDs for the *Herschel* sample ($0.1 < z < 2$) are shown in Fig. 11, split into the three standard luminosity classes: normal IR galaxies (NIRGs; $10^{10} < L_{\rm IR} < 10^{11}$), luminous IR galaxies (LIRGs; $10^{11} < L_{\rm IR} < 10^{12}$) and ultraluminous IR galaxies (ULIRGs; $10^{12} < L_{\rm IR} < 10^{13}$); see Section 3 for details on the SED fitting. The *Herschel* bands cover the bulk of the far-IR emission for the majority of sources, although in some cases the exact position of the SED peak might be underestimated or the slope of the mid-IR continuum might not be well constrained due to lack of data between 24 μm and the first *Herschel* band used in the fitting ($\lambda_{\rm obs} = 100$ or 160 μm). Nevertheless, in all cases the grey-body function covers the bulk of the dust emission giving a good representation of the average temperature of the sources.

To quantitatively describe the global SED shape, we use the $\mathcal{F}$ parameter defined in Section 3. Fig. 12 shows the distribution of $\mathcal{F}$ for the *Herschel* sample, split into the three luminosity classes and overlaid on the distribution of all templates in the SK07 library. Interestingly, the $\mathcal{F}$ distributions of NIRGs, LIRGs and ULIRGs show large overlap, perhaps surprising as one might expect ULIRGs to exhibit a noticeable offset to larger $\mathcal{F}$ values, simply because they are more luminous. However, this is not the case, indicating that many of the *Herschel* ULIRGs are described by cool/extended rather than warm/compact SEDs, in order to reach the same radiation strength per unit area as their lower luminosity counterparts. Indeed, the majority of objects have $8.5 < \mathcal{F} < 10$, suggesting that the IR-luminous population up to $z \sim 2$ is best described by extended rather than compact dust emission. Note that the $\mathcal{F}$ distribution of the *Herschel* sample covers only a small range of the available parameter space. We find that templates with $\mathcal{F} > 11$ are not representative of any object (within the 1σ uncertainties on $\mathcal{F}$) and in fact, only about a 1/3 of the number of templates in the SK07 library are representative of the sample. This provides useful insight on what SED types are observationally confirmed in the context of a physically motivated suite of models.

Fig. 13 illustrates that the observed distribution of $\mathcal{F}$ translates to broad-peaked SEDs for the *Herschel* sample, particularly evident when comparing to those of well-studied local galaxies such as NGC 1808, M82, NGC 6240 and Arp 220 (their SEDs all taken from SK07). For the *Herschel* SEDs, the slope on either side of the peak is shallow in antithesis with the SEDs of the more compact starbursts M82 and Arp 220, which have $\mathcal{F} = 10$ and 11, respectively.

6.2 Far-IR colours

Fig. 14 shows the rest-frame L_{100}/L_{250} versus L_{70}/L_{100} colours of the best-fitting SK07 models to the *Herschel* sample. These bands were chosen for two reasons: (i) they probe a part of the SED that is well sampled by our data hence substantially constraining the SK07 models in that region and (ii) they trace the shape of the SED both around the peak (L_{70}/L_{100}) and in the Rayleigh–Jeans side of the continuum (L_{100}/L_{250}). For comparison, we also include the colours of the SK07 library as well as those of nearby galaxies and modelled SEDs computed using the GRASIL code (Silva et al. 1998).[4] These are: M100, M82, M51, NGC 6946, Arp 220 and NGC 6090, nearby LIRGs and ULIRGs (Vega et al. 2008), modelled colours to represent face-on spirals (Sa, Sb and Sc), as well as high redshift gamma-ray burst (GRB) host galaxies (Michałowski et al. 2008), in essence young, compact, star-forming systems of low metallicity. Nearby LIRGs and ULIRGs, such as M82 and Arp 220, show warm colours, whereas M51, M100 and M6946 are in the cold part of colour–colour space. On the other hand, GRB hosts have similar

[4] http://adlibitum.oat.ts.astro.it/silva/grasil/modlib/modlib.html

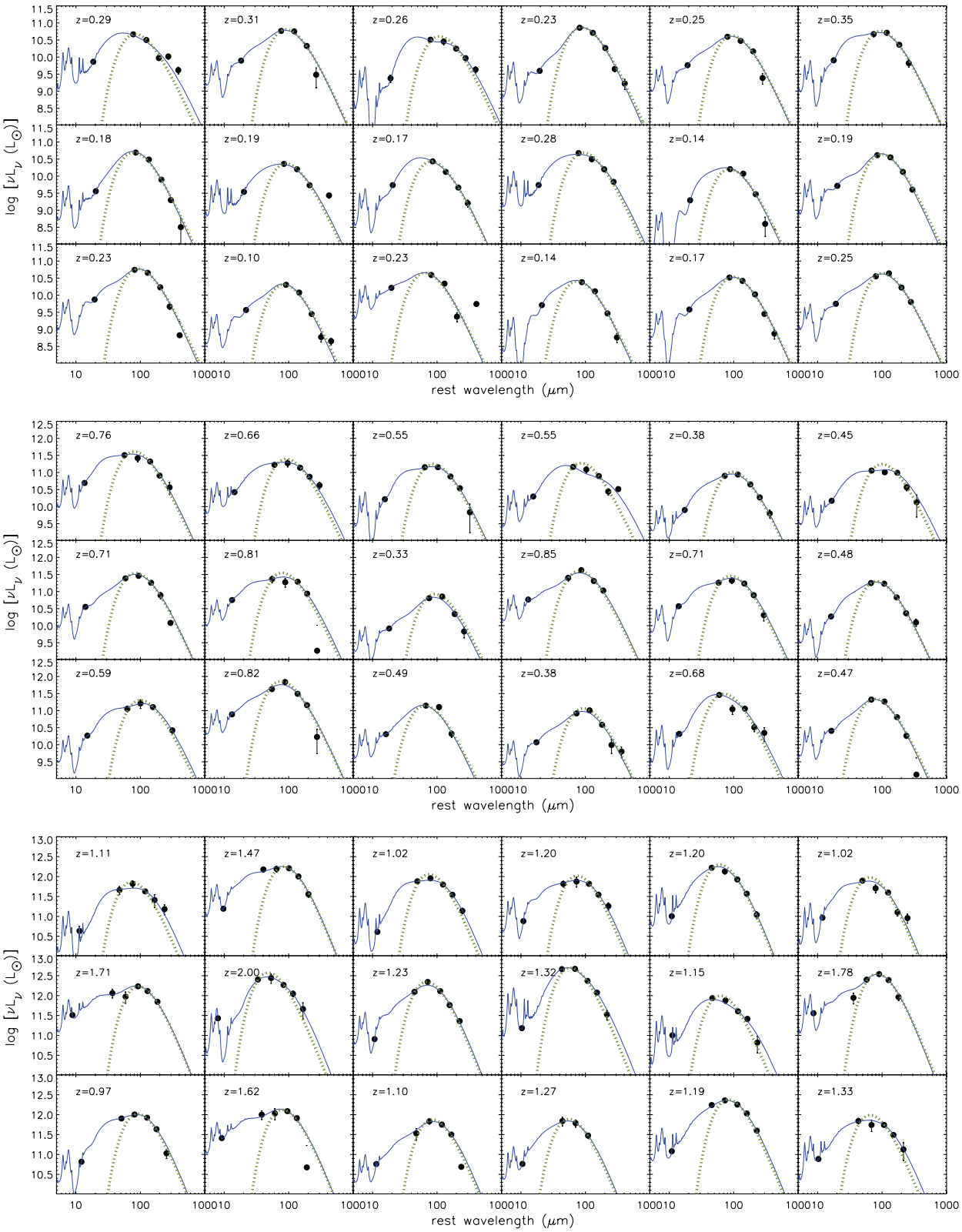

Figure 11. Typical SEDs for NIRGs, LIRGs and ULIRGs; *y*-axis rest-frame luminosity in $L_{\odot}$, *x*-axis rest-frame wavelength (μm). The black points denote the available photometry from 24 to 500 μm. The blue curve shows the best-fitting SK07 model and the green dotted curve shows a single temperature grey-body fit around the photometric peak in νf_{ν}.

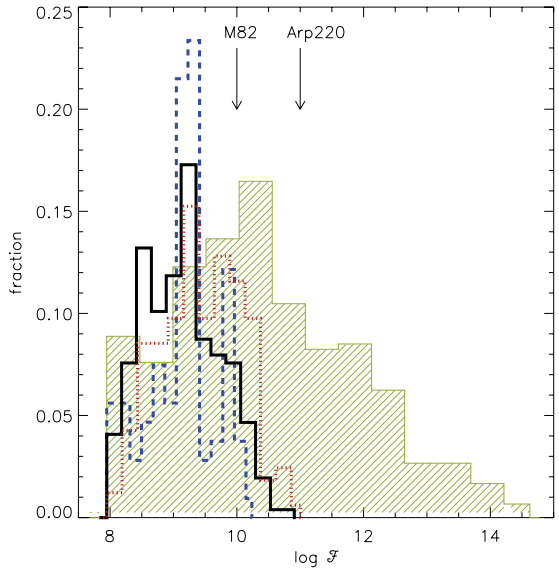

Figure 12. The distribution of $\mathcal{F}$ (log $[L_{\rm tot}/4\pi R^2]$ in units of $L_\odot$ kpc^{-2}) for NIRGS (blue dashed line), LIRGs (black solid line) and ULIRGs (red dotted line). The hatched green region indicates the range covered by the SK07 library. The arrows indicate the value of $\mathcal{F}$ for M82 and Arp 220 (taken from SK07).

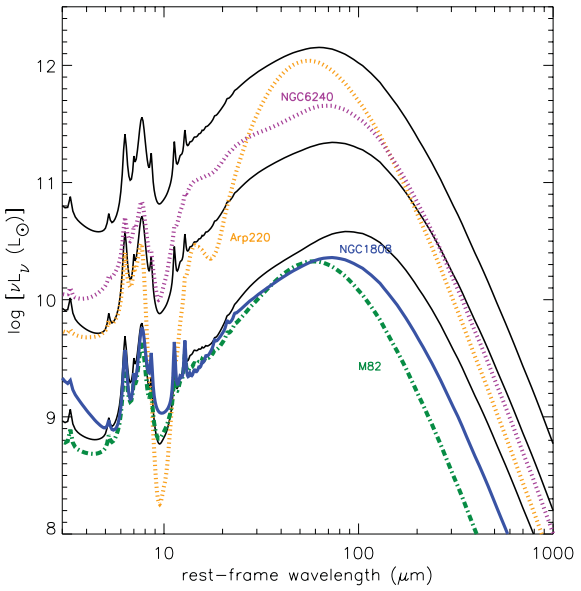

Figure 13. Average SEDs for the *Herschel* sample (black curves) for NIRGs, LIRGs and ULIRGs, from bottom to top, respectively. For comparison we also show the SEDs of Arp 220, NGC 62040, M82 and NGC 1808 taken from SK07.

values of L_{100}/L_{250} but warmer L_{70}/L_{100} colours than spiral galaxies. Note that the modelled spirals (Sa, Sb and Sc) are located along the edge of the available parameter space with colours that become colder down the sequence from Sa to Sc. Although the colours of the Sc spiral are slightly offset from the parameter space that the SK07 templates cover, small discrepancies between SED libraries are expected, particularly since there are many input parameters which can contribute to the final SED shape.

Overall, the SK07 templates extend over a large range in colour–colour space, adequately covering the colours of the comparison sample. The SK07 colours show a large spread below $L_{100}/L_{250} \sim 10$ and a narrow tail at large values of L_{100}/L_{250} and L_{70}/L_{100}. This tail, formed by models with $\mathcal{F} > 11$, is not populated by any of the galaxy groups presented here, suggesting that such hot SEDs are not typical of any type of star-forming galaxy. The darker grey shaded region consists of templates with $9 < \mathcal{F} < 10$ and is the parameter space that most *Herschel* sources occupy (see Fig. 12). These templates have cool far-IR L_{100}/L_{250} colours of <20 and a large spread in L_{70}/L_{100}. A value of $L_{70}/L_{100} = 1.0 \pm 0.3$ ties in with an SED peak between 70 and 100 μm, the range seen in the *Herschel* sample (see Section 6.3). The light grey lower-left part of colour–colour space is scarcely occupied by the *Herschel* sample, indicating that very cold, cirrus-dominated SEDs with $L_{100}/L_{250} < 3$ are uncommon in $L_{\rm IR} > 10^{10}$ $L_\odot$ galaxies. This is not a consequence of either the selection or the survey flux limits; we remind the reader that our sample is complete with respect to the SED types that can be probed. Hence, a deeper IR survey is not expected to identify IR-luminous galaxies with different SEDs to the ones observed here. Colder colours ($L_{100}/L_{250} < 3$) might perhaps be more common amongst more quiescently star-forming galaxies with lower infrared luminosities ($L_{\rm IR} < 10^{10}$ $L_\odot$), but examining such sources is beyond the scope of this paper.

It is interesting to compare the locus of *Herschel* sources with that of the comparison samples. We see significant overlap overall; however, many *Herschel* LIRGs and ULIRGs are clearly offset from the region traditionally occupied by their local counterparts, displaying colder colours consistent with more quiescent star-forming galaxies such as M100 and NGC 6090.

6.3 The luminosity–dust temperature relation

The dust temperature (T) for the *Herschel* sample, derived as described in Section 3, is shown in Fig. 15 as a function of total infrared luminosity. Note that although the derivation of single average dust temperatures represents simplistic assumptions with respect to dust properties, such as optical depth, emissivity, dust geometry and so on, it is currently the only consistent way to characterize and compare statistically large samples of IR-luminous galaxies over a large redshift range.

The mean temperature of the *Herschel* sample ranges from about 28 to 39 K, increasing with $L_{\rm IR}$ and showing an average 1σ scatter of 5 K; see Table 2. Our results confirm that the choice of temperature range (∼18–52 K) over which our sample was described as unbiased (Section 5) was adequate, as we find that the minimum and maximum average temperatures are offset by about 10 K from 18 and 52 K, respectively. In fact, IR-luminous galaxies with $T < 25$ K and $T > 45$ K constitute ∼6 and ∼3 per cent of the total population, respectively.

Since the emission from large dust grains in equilibrium, hence the bulk of the IR emission, is well approximated by the blackbody (or grey-body) function, we also investigate to what extent we can use the Stefan–Boltzmann law, $L = A\epsilon\sigma T^4$, to interpret the $L-T$ relation, where A is the surface area, ϵ is the emissivity and σ is the Stefan constant. A is proportional to R^2, which is in turn proportional to the dust mass ($M_{\rm dust}$), for constant extinction, so one can re-write the Stefan–Boltzmann law as $L \propto M_{\rm dust}T^4$ (or $L \propto R^2T^4$). This spawns two limiting scenarios. The first is that the emitting area and/or dust mass is constant which would result in an $L-T$ relation of the form: $L \propto T^4$. The second is that the emitting area and/or dust mass is proportional to the luminosity ($L \propto R^2$ or $L \propto M_{\rm dust}$) with the temperature remaining constant for all galaxies. The curves representing these scenarios are plotted in Fig. 15. The observed

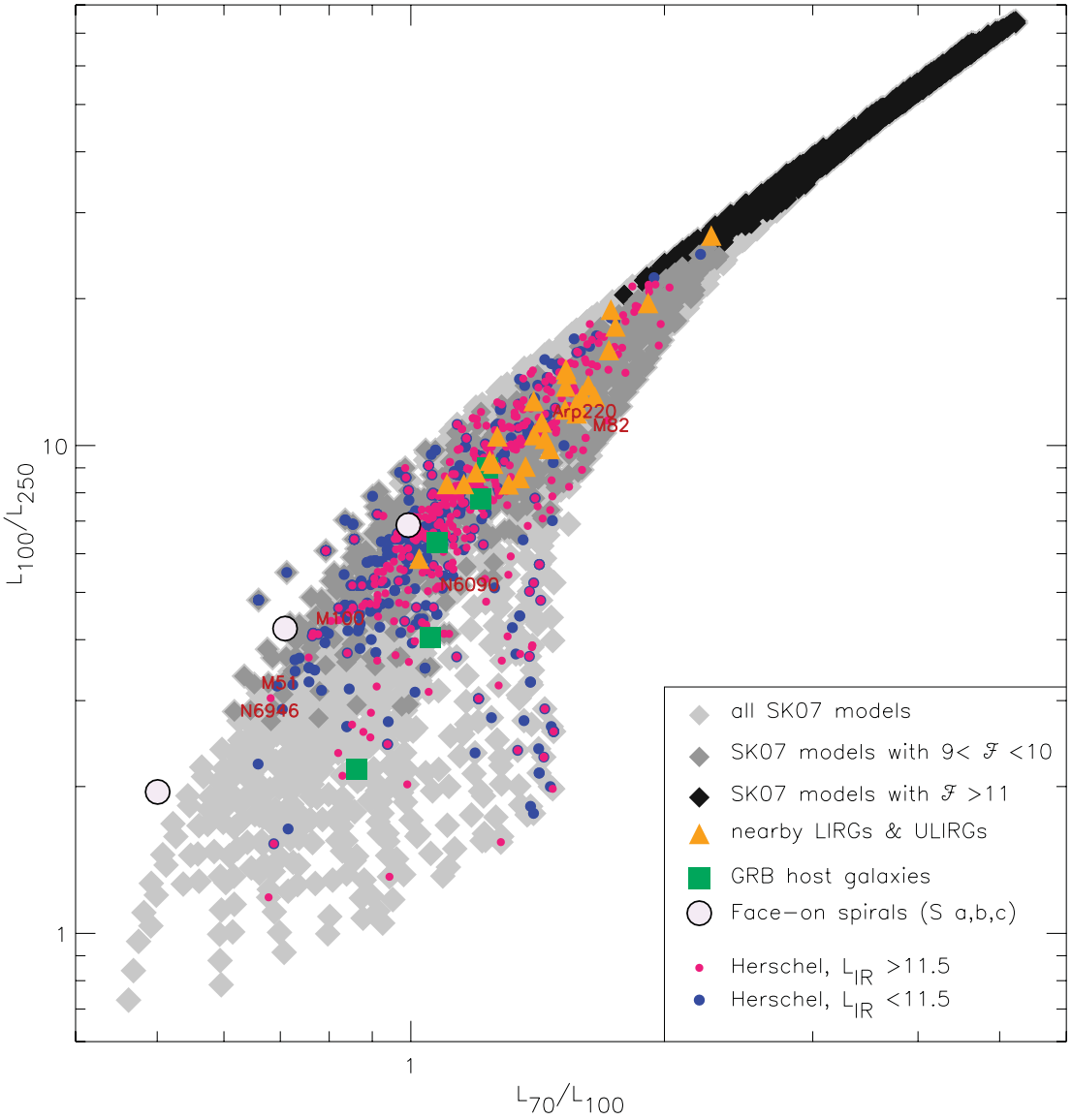

Figure 14. Rest-frame L_{100}/L_{250} versus L_{70}/L_{100} colours for the *Herschel* sample compared to other star-forming galaxy types indicated in the legend. The light grey shaded region represents the colours for the SK07 library, with dark grey shading used for templates of $9 < \mathcal{F} < 10$ and black shading for templates with $\mathcal{F} > 11$. The location of face-on spirals (large white circles with black border) shifts from top right to bottom left with consecutive morphological class, with Sa being in the top right. The red writing indicates the position of the well-known galaxies M100, M82, M51, NGC 6946, Arp 220 and NGC 6090.

$L-T$ relation for the *Herschel* sample is quite flat – a two orders of magnitude increase in luminosity results in only a 40 per cent increase in temperature – and hence closer to the $L \propto M_{\rm dust}$ limiting scenario. This suggests that the $L-T$ relation is mainly shaped by an increase in dust mass and/or IR emitting radius and less so by an increase in dust heating. In other words, the average dust temperature of ULIRGs is much lower than what one would expect if their increased luminosity were the only factor shaping the $L-T$ relation. This indicates that the dust masses and/or sizes of ULIRGs are larger than those of NIRGs, significantly diluting the effect that their increased luminosity has on the temperature.

Fig. 16 shows the $L-z$ distribution of the sample, split into bins of 0.2 dex in luminosity and 0.2 in redshift. For the bins additionally outlined in red (24 in total), containing $\geq$5 objects, we compute the average SED in that bin shown in Fig. 17. Fig. 17 is analogous to Fig. 16, such that each row represents a change in redshift interval, and each column a change in luminosity interval. The shaded region represents the 1σ scatter around the average SEDs, whereas the red SED at the end of each row is the average for that row. Consistent with what we observe with regard to the $L-T$ relation (Fig. 15), Fig. 17 demonstrates that there is a shift in the SED peak from longer to shorter wavelengths with increasing infrared luminosity. This is more clear in the last column which shows the average SED for each luminosity bin: the SED peak ($\lambda_{\rm peak}$) shifts from 86 μm in the lowest luminosity bin to 65 μm in the highest luminosity bin. This is also seen in Fig. 13 where the average SED of each luminosity class is shown, with the mean and standard deviation in $\lambda_{\rm peak}$ being 86±18 μm for NIRGs, 75±18 μm for LIRGs and 65±17 μm for ULIRGs. Note that the 1σ scatter is large, partly because the peak is not always well constrained by our data, and partly

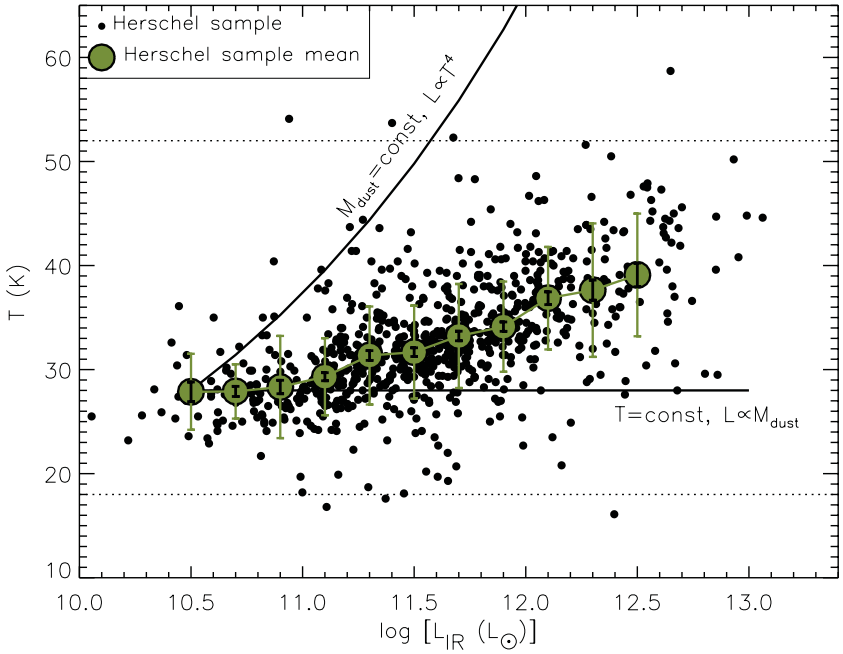

Figure 15. Dust temperature as a function of total infrared luminosity for the *Herschel* sample (black points). The green filled circles denote the mean temperatures computed for 11 L_{IR} bins (see Table 2). The green error bars show the standard deviation in the measured temperatures of each bin, whereas the black error bars denote the error on the mean. The two limiting scenarios of the Stefan–Boltzmann law are also shown (solid black lines). The dotted horizontal lines outline the $L-T$ parameter space in which we are complete; see Section 5.1.

because of the large diversity in SED types (see Figs 11 and 14 for examples).

Another feature that appears to change with L_{IR} is the silicate absorption depth, becoming shallower for higher L_{IR}. Our data do not probe the depth of the silicate feature, except over a small window in redshift where it coincides with the 24 μm passband. Hence, this trend is likely an artefact brought about by model degeneracies. In the SK07 formulation, visual extinction is tied in to the silicate absorption depth, the slope of the mid-IR continuum and the SED peak wavelength. These quantities are significantly degenerate at low redshifts, although for high-redshift sources ($z \gtrsim 1$), the photometry probes further into the mid-IR continuum, placing additional constraints on the extinction. Nevertheless, although the SED shape in the near/mid-IR is more reliably reproduced for the high-redshift sources, the observed trend of decreasing silicate depth with increasing L_{IR} is most likely artificial.

Table 2. The mean temperature, 1σ scatter per L_{IR} bin and error on the mean for the *Herschel* sample – see Fig. 15. The last column shows the median redshift of each L_{IR} bin.

log L_{IR} ($L_\odot$)	Mean T (K)	1σ (K)	Error on mean T (K)	Median z
10.4–10.6	27.9	3.7	0.94	0.14
10.6–10.8	27.9	2.6	0.48	0.19
10.8–11	28.3	4.9	0.64	0.23
11–11.2	29.3	3.7	0.39	0.36
11.2–11.4	31.4	4.7	0.47	0.42
11.4–11.6	31.7	4.5	0.42	0.54
11.6–11.8	33.2	5	0.46	0.67
11.8–12	34.1	4.3	0.45	0.84
12–12.2	36.9	4.9	0.62	0.94
12.2–12.4	37.6	6.4	0.97	1.09
12.4–12.6	39.1	5.9	1.13	1.23

6.4 Evolution in dust conditions

In Fig. 18, we compare the properties of the *Herschel* sources to those of the local sample, assembled as described in Section 5.3. The local luminosity–temperature and luminosity–colour (C; L_{60}/L_{100}) relations, the latter in functional form from Chapin et al. (2009), are shown in Fig. 18, left- and right-hand panels, respectively. The L_{60}/L_{100} colour has been used extensively to characterize the dust temperature of local samples, and an analysis of *IRAS*-selected galaxies has shown that more luminous sources have higher colour temperatures than their less luminous counterparts (e.g. Dunne et al. 2000; Dale et al. 2001; Dale & Helou 2002; Chapman et al. 2003). For both $L-T$ and $L-C$ relations we note a systematic difference between the *Herschel* and local samples, with the former displaying lower values of T and L_{60}/L_{100}. This can be interpreted as evidence for evolution: high-redshift IR-luminous galaxies have more emission longwards of ∼60 μm compared to their low-redshift analogues, lowering the average dust temperature. This is consistent with results from Section 6.2, Fig. 14, where we see that the *Herschel* sample extends to colder far-IR colours than local LIRGs and ULIRGs.

Recent results from the Planck Collaboration (2011, Part 16) on the dust properties of nearby *IRAS*-selected sources showed that many local $10^{10} < L_{IR} < 10^{11}$ galaxies extended to lower temperatures than previously reported. This does not affect our work as (i) within the scatter and given that emissivity is a free parameter in their fitting, their measured dust temperatures in the $10^{10} < L_{IR} < 10^{11}$ luminosity range are consistent with the ones we report here for the local sample (Fig. 18) and (ii) as described in Section 5.3, we assemble the local sample in an unbiased part of parameter space. Furthermore, lack of additional submm/mm data for our nearby sources would not change the average dust temperatures measured,

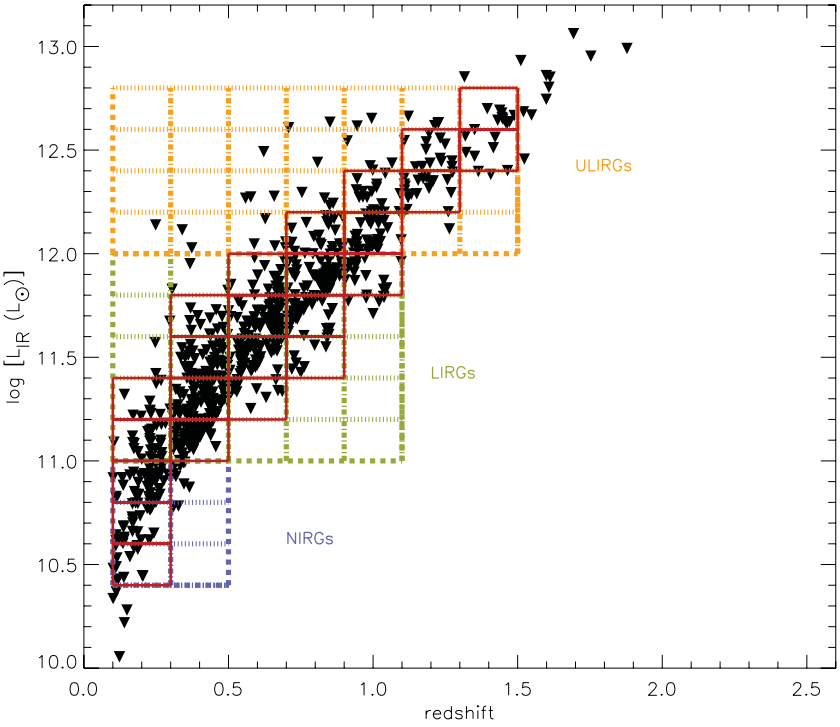

Figure 16. The luminosity–redshift parameter space of the final *Herschel* sample used in the analysis (black triangles), split into bins of size 0.2 dex in luminosity and 0.2 in redshift. The bins are outlined in blue for NIRGs, green for LIRGs and orange for ULIRGs and further delineated in red if used when computing the average SED shape in that bin (see Fig. 17 for average SEDs).

as these trace the peak dust emission and are thus insensitive to inclusion of photometry significantly longwards of the peak (see also Magnelli et al. 2012).

Although a systematic reduction in the dust temperature and colour of IR-luminous galaxies from the local to the high-redshift Universe is observed, it is worth examining how this translates to changes in the SED shape with redshift within the *Herschel* sample. In Fig. 17, we see some evidence for a shift in the SED peak to longer wavelengths along the rows, i.e. with increasing redshift, for example in the $\log L_{\rm IR} = 11.4$–11.6 bin. However, overall, it is not clear how the SED shape evolves with redshift. This is likely a consequence of sparse sampling of the SK07 templates by our photometry, exacerbated by the small redshift range covered along each row, statistical uncertainties in each bin as well as the fact that in many cases, sources do not cover each $L-z$ bin uniformly (see Fig. 16). A different way to investigate evolution in dust properties is to repeat this exercise with our computed dust temperatures, in order to remove model-dependent uncertainties, although the other sources of uncertainty outlined above would remain. Fig. 19 shows a 2D image of the dust temperature of IR luminous galaxies (local and *Herschel* samples combined) as a function of redshift and luminosity, in bins of 0.2 and 0.2 dex, respectively. Besides an increase in average dust temperature vertically along the luminosity axis, consistent with our analysis in Section 6.3 on the $L-T$ relation, we also note an overall reduction in the mean dust temperature, horizontally, along the redshift axis. This is more pronounced when considering the first and last bins of each row; however, in some cases it is also evident along the length of the row.

Considering the above trends, it is interesting to examine whether the evolution in dust temperature we observe is luminosity dependent, i.e. whether dust conditions of ULIRGs evolve at a different rate to those of NIRGs (Fig. 20). We place the separation between cold and warm at $T = 35$ K, corresponding to the mean temperature for the *Herschel* sample shown in Fig. 18. Fig. 20 shows an increase in the fraction of cold ULIRGs with redshift, from 5 per cent in the local Universe to about 30 per cent at $z \sim 1$–2. Also the fraction of cold LIRGs increases from about 60 per cent locally to about 80 per cent at high redshift. However, as for Figs 17 and 19, in some bins, the $L-z$ parameter space is not sampled uniformly. The higher redshift bins in Fig. 20 include a larger fraction of more luminous and hence warmer sources, implying that the fraction of cold sources is likely underestimated, resulting in the observed downturn of the computed fraction.

Note that given the depth of our data, currently this is the best attainable coverage of the $L-z$ plane in the horizontal (z) direction within the unbiased framework we define in this work. This does not mean that LIRGs at $z \gtrsim 1$ and ULIRGs at $z \gtrsim 2$ will not be detected by *Herschel* or other facilities, rather it implies that it is not currently possible to measure the *aggregate* properties of the LIRG and ULIRG population at those redshifts. On the other hand, with larger area *Herschel* surveys we expect to cover the gap between the local and high-redshift Universe in the vertical (L) direction, enabling better sampling of the $L-z$ plane, where large survey area is needed, and hence achieve better statistics for $\log L_{\rm IR}/{\rm L}_{\odot} > 11.5$ galaxies up to $z = 1$.

With respect to the selection at 24 μm, we saw that we are likely missing a few per cent of SEDs with steep far-to-mid-IR continua and deep silicate features, about half of which have $f_{500}/f_{160} > 1$ extending to higher values than we find in the *Herschel* sample (see Fig. 8 and Section 5.2). This suggests that many of the sources missed by the 24 μm criterion might have lower temperatures than the average temperatures derived for the *Herschel* sample. Although

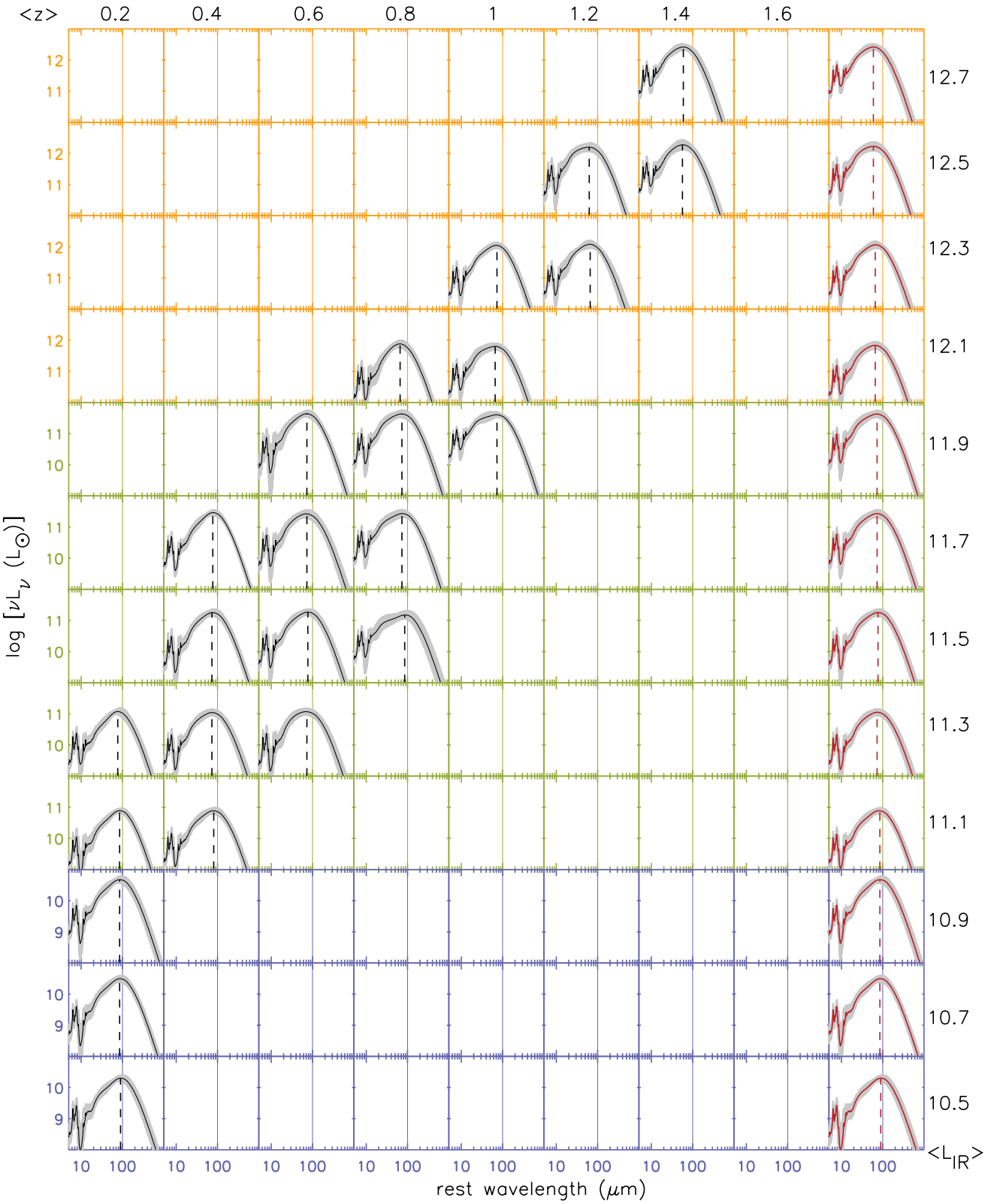

Figure 17. Average SEDs (νL_ν versus $\lambda_{\rm rest}$) for the *Herschel* sample. This figure is analogous to Fig. 16, such that each row represents a change in redshift interval and each column a change in luminosity interval. The central luminosity and redshift of each bin are shown on the left-hand side and top of the plot, respectively. Average SEDs are shown for $L-z$ bins with five or more objects, outlined in red in Fig. 16. The boxes are coloured blue for NIRGs, green for LIRGs and orange for ULIRGs. The solid vertical line in the middle of each box is at 100 μm, whereas the dashed line denotes the SED peak. The red SEDs at the end of each row are the average SEDs for that row.

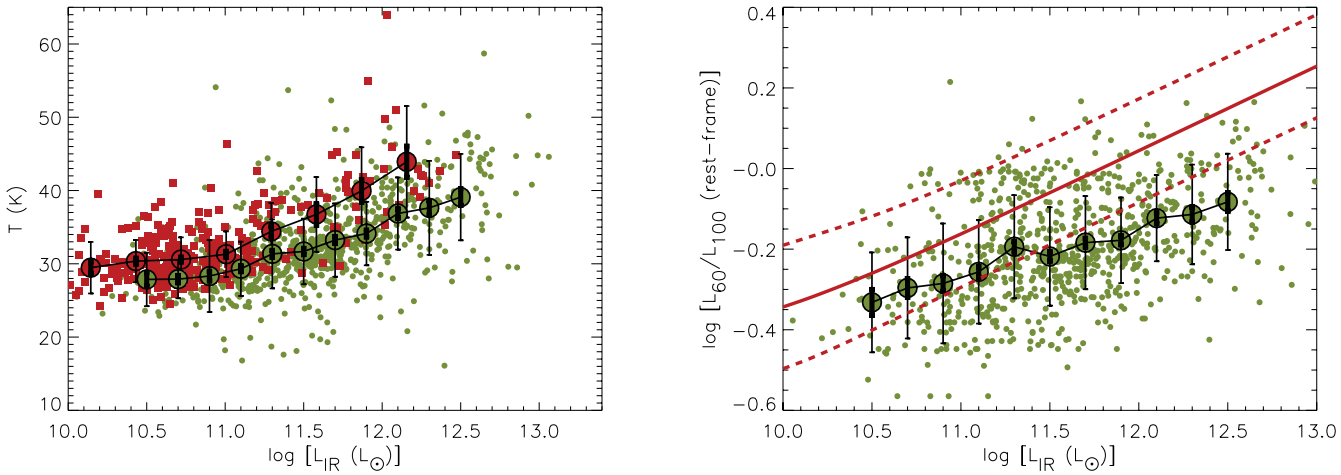

Figure 18. Left-hand panel: dust temperature versus $L_{\rm IR}$ for the *Herschel* sample (green circles) and the local ($z \lesssim 0.1$) sample (red squares). The mean trends for the two samples are also shown (large filled circles) with the large thin error bars representing the 1σ scatter in each bin and the short thick error bars representing the error on the mean. Right-hand panel: rest-frame colour (L_{60}/L_{100}) as a function of total infrared luminosity for the *Herschel* sample (green circles). The large filled circles represent the mean trend with the large thin error bars representing the 1σ scatter in each bin and the short thick error bars representing the error on the mean. The solid and dashed lines denote the local luminosity–colour relation and 1σ limits from Chapin, Hughes & Aretxaga (2009).

this fraction of sources is very small and hence unlikely to change our results, it would nevertheless only serve to strengthen the differences we observe between the local and high-redshift sample.

7 DISCUSSION

7.1 The properties of the IR-luminous population

The *Herschel* sample under study consists mainly of LIRGs (64 per cent), with ULIRGs constituting 20 per cent, consistent with what is expected in the redshift range probed ($0.1 < z < 2$), whereas the remaining 16 per cent are NIRGs ($10^{10} < L_{\rm IR} < 10^{11}$ L$_\odot$). The dust temperatures of the sample show large scatter from 15 to 55 K; however, the mean temperature ranges from 28±4 to 39±6 K, with ULIRGs being on average about 10 K warmer than NIRGs. Similarly, we see a shift in the average SED peak wavelength from 86±18 μm for NIRGs to 65±17 μm for ULIRGs. The sample is best described by cool/extended rather than warm/compact SEDs and broad peaks, translating to low values of $\mathcal{F}$, a parameter which we defined as a measure of the overall IR SED shape. In addition, there is a large overlap in colour–colour (L_{100}/L_{250}–L_{70}/L_{100}) space between the *Herschel* sample and other star-forming galaxy types, the coldest of which (spirals and young compact star-forming galaxies) are at $L_{100}/L_{250} \lesssim 7$ and the warmest (ULIRGs and starbursts) at $L_{100}/L_{250} \gtrsim 7$. For the *Herschel* sample, we noted a roughly equal number of sources above and below $L_{100}/L_{250} \sim 7$. It is worth mentioning that only about a 1/3 of the SK07 templates are representative of the *Herschel* sample. The $L_{100}/L_{250} > 20$, $L_{100}/L_{250} < 3$ and $L_{70}/L_{100} > 2$ regions of the SK07 library are scarcely populated. Moreover, the distribution of $\mathcal{F}$ of the SK07 library extends to much higher values ($\mathcal{F} \sim 15$) than what is observed in the *Herschel* sample ($\mathcal{F} < 11$). This indicates that compact, hot-dust-dominated SEDs or very cold cirrus-dominated SEDs are not typical of the IR-luminous population.

How do our findings compare to other studies of IR galaxies? As mentioned earlier, we have performed a rigorous analysis of selection effects in order to minimize any biases which would interfere with our results. Hence, due to the nature of our study, we are sensitive to most, if not all, IR galaxy types with $L_{\rm IR} > 10^{10}$ L$_\odot$ at $z = 0.1$–2. Consequently, results on the properties of IR galaxies from previous studies with *Spitzer* (e.g. Symeonidis et al. 2009; Kartaltepe et al. 2010a; Patel et al. 2011) and SCUBA (e.g. Kovács et al. 2006; Coppin et al. 2008; Santini et al. 2010) are all within the parameter space we probe (see also Magnelli et al. 2012). The results reported recently using *Herschel* data (e.g. Hwang et al. 2010; Rowan-Robinson et al. 2010; Smith et al. 2012) are also within the parameter space we define here for the IR-luminous population. However, we note that although cold, cirrus-dominated SEDs such as those reported in Rowan-Robinson et al. (2010) and Smith et al. (2012) are part of our sample, they represent a small fraction (<6 per cent) of the IR-luminous population and are not the prevalent SED types.

7.2 The $L-T$ relation

The increase in dust temperature as a function of infrared luminosity we observe here is similar to the $L-T$ relation that has emerged from most infrared population studies (e.g. Dunne et al. 2000; Dale et al. 2001; Dale & Helou 2002; Chapman et al. 2003). Since the emission from large dust grains in equilibrium, hence the bulk of the IR emission, is well approximated by a black (or grey) body function, we aimed to understand the $L-T$ relation within the framework of the Stefan–Boltzmann law. As described in Section 6.3, the two limiting scenarios of the Stefan–Boltzmann law are: (i) $L \propto T^4$ with R (the radius of the emitting region), or $M_{\rm dust}$ (the dust mass) kept constant and (ii) $L \propto R^2$ or $L \propto M_{\rm dust}$ with T kept constant. The former scenario would produce a steep $L-T$ relation, whereas for the latter the $L-T$ relation would be flat, with the increase in luminosity tying in with an increase in surface area of the emitting body or the dust mass. We find that the $L-T$ relation for the *Herschel* sample lies closer to the latter scenario suggesting that its shape is mainly driven by an increase in dust mass or extent of dust emitting region and less so by energetics. In other words, it seems that the increased dust heating in ULIRGs is diluted by an increase

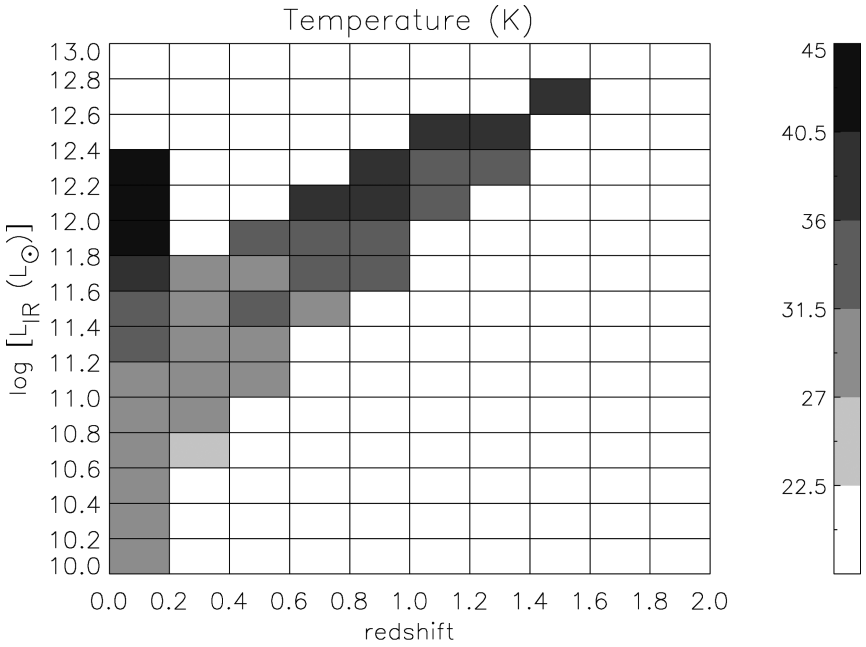

Figure 19. 2D image of the $L-T-z$ space for IR-luminous galaxies from the local Universe to $z = 2$. This includes both the local and the *Herschel* samples. Objects are divided into $L_{\rm IR}$ (y-axis) and z bins (x-axis), and the average temperature of each bin is shown as a grey-scale intensity map. The colour bar on the right is the temperature key for the map. The temperature bins extend from 22.5 to 45 K. White colour indicates unpopulated or underpopulated (i.e. <5 objects) $L-T-z$ bins.

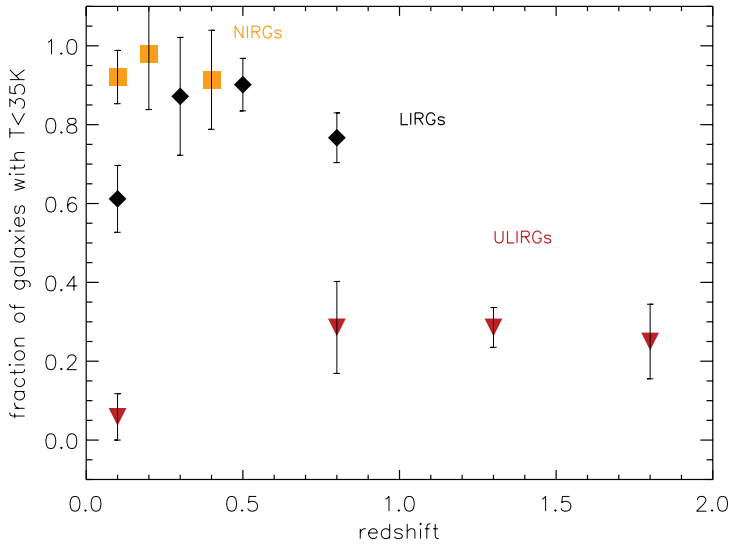

Figure 20. The fraction of T <35 K NIRGs (orange squares), LIRGs (black diamonds) and ULIRGs (red triangles) as a function of redshift. The local sample is at $z \sim 0.1$ and the remaining bins include sources from the *Herschel* sample only.

in their physical size and/or dust mass, such that the $L-T$ relation is diverted away from the $L \propto T^4$ scenario. However, although more strongly star-forming galaxies such as ULIRGs are predominantly more massive (e.g. Davé 2008; Shapley 2011) and dustier systems (e.g. Magdis et al. 2012) with warmer average dust temperatures, we find that their SED shapes are not substantially different to their lower luminosity counterparts. In particular, we do not see a clear segregation in the far-IR colour–colour space or in the range covered by $\mathcal{F}$ as a function of infrared luminosity. Interestingly, this suggests that properties such as optical depth, dust extinction, extent of IR emitting regions, etc. which determine the overall SED shape are not substantially different between high-redshift ULIRGs and lower luminosity equivalent systems.

7.3 Evolution of the IR-luminous population

In this work we found evidence that the dust temperatures of *Herschel* sources are systematically colder than equivalently luminous galaxies in the local Universe. The rigorous analysis of survey biases we performed ensures the validity of this result, as our final sample selection was sensitive to all IR galaxies with $18 \lesssim T(\mathrm{K}) \lesssim 52$. We found sources at $z > 0.5$ and $\log [L_{\rm IR}/\mathrm{L}_\odot] > 11.0$ to be on average between 5 and 10 K colder than their $z < 0.1$ counterparts. We also noted a systematic offset towards colder rest-frame L_{60}/L_{100}, L_{100}/L_{250} and L_{70}/L_{100} colours for the *Herschel* sample in comparison to local equivalent sources. We believe that this is unlikely to be due to an increase in extinction, which by removing

flux from the mid-IR and adding it in the far-IR could mimic a lower dust temperature. As discussed earlier, sources with high extinction and deep silicate absorption are missed by our 24 μm selection at $z > 1$. However, they do not constitute more than a few per cent of the population (see also Magdis et al. 2010). Moreover, for the high-redshift sources, where the *Herschel* photometry can more accurately constrain the slope of the mid-IR-to-far-IR continuum, we find that the sample is mainly fitted with low-extinction (shallow silicate absorption depth) models.

Note that although previous studies have shown that IR galaxies colder than local equivalents exist in abundance at high redshift – e.g. results from *ISO* (e.g. Rowan-Robinson et al. 2005), SCUBA (Kovács et al. 2006; Pope et al. 2006; Coppin et al. 2008), *Spitzer* (e.g. Symeonidis et al. 2008, 2009; Kartaltepe et al. 2010a; Patel et al. 2011), *BLAST* (Muzzin et al. 2010), *Herschel* (e.g. Hwang et al. 2010; Rowan-Robinson et al. 2010; Smith et al. 2012) – for the first time we determine that the mean dust temperature of the IR-luminous population as a whole decreases as a function of redshift. Moreover, we find that the decrease in temperature is also a function of infrared luminosity, i.e. the temperatures of more luminous objects show a stronger decline from the local to the early Universe. We note that almost all NIRGs, up to $z \sim 0.5$, have temperatures below 35 K, whereas for LIRGs the local cold ($T < 35$ K) fraction is 60 per cent increasing to about 90 per cent at $z \sim 0.5$. The ULIRGs show the largest increase in the cold galaxy fraction, from about 5 per cent at $z < 0.1$ to 30 per cent at $z = 1-2$. This is interesting as it implies that LIRGs undergo more modest evolution than ULIRGs, the former showing a two-fold increase in the fraction of cold galaxies, whereas the latter a six-fold increase. Moreover, the cold LIRG fraction in the local Universe is about 12 times higher than the cold ULIRG fraction; however, we see that this difference decreases to about 2.5 at $z \sim 0.8$. Similarly the cold NIRG fraction in the local Universe is about 50 per cent higher than the cold LIRG fraction, whereas at $z \sim 0.4$ these fractions are about the same. This is evidence that cold galaxies become more dominant at high redshift. However, it also indicates that there might be a lower limit in the average dust temperature of the IR-luminous population, at $T \sim 25$ K, towards which systems tend. This is not to say that $T < 25$ K IR-luminous galaxies do not exist, but these would be at the tail of the temperature distribution.

As discussed earlier, the $L-T$ relation would be completely flat, e.g. all IR luminous galaxies would have an average temperature of ∼25 K, if their sizes or dust masses increased in proportion to their total IR luminosities (see also Fig. 15). As it stands, this is not the case, and so the increased luminosity succeeds in heating up the dust to a higher temperature. However, the decrease in average dust temperature with redshift suggests that high-redshift LIRGs/ULIRGs must have more extended IR emitting regions and/or higher dust masses relative to their lower redshift counterparts, causing the $L-T$ relation at high redshift to become flatter than the local one. Described phenomenologically, we observe that the temperature evolution of IR-luminous galaxies is more rapid if their local temperatures are much higher than 25 K, such as for ULIRGs, than if they are closer to 25 K such as for NIRGs. Our results are in agreement with the work presented in Dunne et al. (2011) who find strong evolution in the dust mass density, proposing that IR-luminous galaxies are dustier at $z \sim 0.5$ compared to today, corresponding to a factor of 4–5 increase in the dust masses of the most massive galaxies. Moreover, CO measurements support the idea of extended instead of compact star formation in high-redshift ULIRGs, which have ≫kpc CO sizes, in contrast to local equivalent sources which are more concentrated (<1 kpc) (e.g. Tacconi et al. 2006; Iono et al. 2009; Rujopakarn et al. 2011). Moreover, significantly higher gas fractions in $z \sim 1$ disc galaxies than in nearby discs have been reported (e.g. Tacconi et al. 2010). Our results also agree with Seymour et al. (2010), who studied the comoving IR luminosity density (IRLD) as a function of temperature, proposing that cold galaxies dominate the IRLD across $0 < z < 1$ and are thus likely to be the main driver behind the increase in SFR density up to $z \sim 1$.

Although the IR-luminous population and particularly LIRGs and ULIRGs seem to have more extended dust distribution and/or higher dust masses at high redshift, the analysis presented here cannot constrain whether these systems are characterized by a merger-induced or isolated star-formation history or where they are located in the SFR–stellar mass parameter space (e.g. Reddy et al. 2006, 2010; Wuyts et al. 2011; Whitaker et al. 2012; Zahid et al. 2013). Morphological studies of IR-luminous galaxies have presented contrasting results – e.g. Bell et al. (2005) and Lotz et al. (2006) report that more than half of LIRGs at $z > 0.7$ are gas-rich isolated spirals, whereas other studies (e.g. Le Fevre et al. 2000; Cassata et al. 2005; Bridge et al. 2007; de Ravel et al. 2009) claim an increase in the merger rate out to $z \sim 1$ suggesting that more than half of IRLD out to $z \sim 1$ is a result of some merger event. Moreover, Zamojski et al. (2011) and Kartaltepe et al. (2012) find more than 70 per cent of ULIRGs up to $z \sim 2$ to be mergers. These findings are difficult to reconcile and recent evidence from Lotz et al. (2011) shows that these differences might simply be the result of increasing gas fractions at high redshift, as the time-scale for observing a galaxy to be asymmetric increases in tandem with the gas fraction, with the resulting dust obscuration also being a key factor. With the work presented here, we are not able to test this argument nor examine the morphological evolution (if any) of IR galaxies. Nevertheless, our description of the IR-luminous population is independent of morphological classification. Our results indicate that the gas-rich environment in the early Universe might have set or enabled different initial conditions in these systems, resulting in the observed differences between IR galaxies at high redshift and their local counterparts. The increase in cold ($T < 35$ K) galaxy fraction reported here suggests a greater diversity in the IR population at high redshift, particularly for (U)LIRGs. In contrast, the dust properties of the local (U)LIRG population are more uniform and as a result they are not archetypal of the (U)LIRG population as a whole.

8 SUMMARY AND CONCLUSIONS

We have examined the dust properties and infrared SEDs of a sample of 1159 infrared-selected galaxies at $z = 0.1$-2, using data from *Herschel*/PACS and SPIRE and *Spitzer*/MIPS (24 μm) in the COSMOS and GOODS (N+S) fields. The unique angle of this work has been the rigorous analysis of survey selection effects, enabling us to work within a framework almost entirely free of selection biases. The results we thus report should be considered as representative of the aggregate properties of the star-formation-dominated, IR-luminous ($L_{\rm IR} > 10^{10}$) population up to $z \sim 2$.

We conclude that:

(i) IR-luminous galaxies have mean dust temperatures between 25 and 45 K, with $T < 25$ and $T > 45$ K sources being rare. They are characterized by broad-peaked and cool/extended rather than warm/compact SEDs; however, very cold cirrus-dominated SEDs are rare occurrences, with most sources having SED types between those of warm starbursts such as M82 and cool spirals such as M51.

(ii) The IR luminous population follows a luminosity–temperature ($L-T$) relation, where the more luminous sources have up to 10 K higher dust temperatures. However, the effect of increased dust heating is not solely responsible for shape of the $L-T$ relation. We find that the increase in dust mass and/or extent of dust distribution of the more luminous sources dilutes the increased dust heating, flattening the $L-T$ relation and driving it towards the limiting scenario of $L \propto R^2$ or $L \propto M_{\rm dust}$ with $T = {\rm const}$.

(iii) High-redshift IR-luminous galaxies are on average colder with a temperature difference that increases as a function of total infrared luminosity and reaches a maximum of 10 K. For the more luminous ($\log[L_{\rm IR}/{\rm L}_{\odot}] \gtrsim 11.5$) sources, the $L-T$ relation is flatter at high redshift than in the local Universe, suggesting an increase in the sizes and/or dust masses of these systems compared to their local counterparts.

(iv) The fraction of $T < 35$ K galaxies increases with redshift as a function of total infrared luminosity. Although NIRG fractions are consistent in the local and high-redshift Universe, LIRGs show a two-fold increase and ULIRGs a six-fold increase. This suggests a greater diversity in the IR-luminous population at high redshift, particularly for ULIRGs.

ACKNOWLEDGEMENTS

This paper uses data from *Herschel*'s photometers SPIRE and PACS. SPIRE has been developed by a consortium of institutes led by Cardiff Univ. (UK) and including: Univ. Lethbridge (Canada); NAOC (China); CEA, LAM (France); IFSI, Univ. Padua (Italy); IAC (Spain); Stockholm Observatory (Sweden); Imperial College London, RAL, UCL-MSSL, UKATC, Univ. Sussex (UK); and Caltech, JPL, NHSC, Univ. Colorado (USA). This development has been supported by national funding agencies: CSA (Canada); NAOC (China); CEA, CNES, CNRS (France); ASI (Italy); MCINN (Spain); SNSB (Sweden); STFC, UKSA (UK); and NASA (USA). PACS has been developed by a consortium of institutes led by MPE (Germany) and including UVIE (Austria); KU Leuven, CSL, IMEC (Belgium); CEA, LAM (France); MPIA (Germany); INAF-IFSI/OAA/OAP/OAT, LENS, SISSA (Italy); IAC (Spain). This development has been supported by the funding agencies BMVIT (Austria), ESA-PRODEX (Belgium), CEA/CNES (France), DLR (Germany), ASI/INAF (Italy), and CICYT/MCYT (Spain).

REFERENCES

Alexander D. M., Smail I., Bauer F. E., Chapman S. C., Blain A. W., Brandt W. N., Ivison R. J., 2005, Nat, 434, 738
Amblard A. et al., 2010, A&A, 518, L9
Armus L. et al., 2007, ApJ, 656, 148
Baugh C. M., Lacey C. G., Frenk C. S., Granato G. L., Silva L., Bressan A., Benson A. J., Cole S., 2005, MNRAS, 356, 1191
Bell E. F. et al., 2005, ApJ, 625, 23
Berta S. et al., 2010, A&A, 518, L30
Berta S. et al., 2011, A&A, 532, A49
Blain A. W., Chapman S. C., Smail I., Ivison R., 2004, ApJ, 611, 52
Bower R. G., Benson A. J., Malbon R., Helly J. C., Frenk C. S., Baugh C. M., Cole S., Lacey C. G., 2006, MNRAS, 370, 645
Brammer G. B. et al., 2008, ApJ, 686, 1503
Brandl B. R. et al., 2006, ApJ, 653, 1129
Bridge C. et al., 2007, ApJ, 659, 931
Buat V. et al., 2010, MNRAS, 409, L1
Cardamone C. N. et al., 2010, ApJS, 189, 270
Cassata P. et al., 2005, MNRAS, 357, 903
Chapin E. L., Hughes D. H., Aretxaga I., 2009, MNRAS, 393, 653
Chapman S. C., Helou G., Lewis G. F., Dale D. A., 2003, ApJ, 588, 186
Choi P. I. et al., 2006, ApJ, 637, 227
Clements D. L., Dunne L., Eales S., 2010, MNRAS, 403, 274
Condon J. J., Huang Z.-P., Yin Q. F., Thuan T. X., 1991, ApJ, 378, 65
Coppin K. et al., 2008, MNRAS, 384, 1597
Dale D. A., Helou G., 2002, ApJ, 576, 159
Dale D. A., Helou G., Contursi A., Silbermann N. A., Kolhatkar S., 2001, ApJ, 549, 215
Davé R., 2008, MNRAS, 385, 147
de Ravel L. et al., 2009, A&A, 498, 379
Desert F.-X., Boulanger F., Puget J. L., 1990, A&A, 237, 215
Dole H. et al., 2006, A&A, 451, 417
Donley J. L. et al., 2012, ApJ, 748, 142
Dunne L., Eales S. A., 2001, MNRAS, 327, 697
Dunne L., Eales S., Edmunds M., Ivison R., Alexander P., Clements D. L., 2000, MNRAS, 315, 115
Dunne L. et al., 2011, MNRAS, 417, 1510
Dye S. et al., 2008, MNRAS, 386, 1107
Dye S. et al., 2010, A&A, 518, L10
Eales S., Lilly S., Gear W., Dunne L., Bond J. R., Hammer F., Le Fèvre O., Crampton D., 1999, ApJ, 515, 518
Eales S., Lilly S., Webb T., Dunne L., Gear W., Clements D., Yun M., 2000, AJ, 120, 2244
Eales S. et al., 2010a, PASP, 122, 499
Eales S. A. et al., 2010b, A&A, 518, L23
Egami E. et al., 2004, ApJS, 154, 130
Farrah D. et al., 2001, MNRAS, 326, 1333
Farrah D., Verma A., Oliver S., Rowan-Robinson M., McMahon R., 2002, MNRAS, 329, 605
Farrah D., Afonso J., Efstathiou A., Rowan-Robinson M., Fox M., Clements D., 2003, MNRAS, 343, 585
Farrah D. et al., 2007, ApJ, 667, 149
Farrah D. et al., 2008, ApJ, 677, 957
Genzel R. et al., 1998, ApJ, 498, 579
Giavalisco M. et al., 2004, ApJ, 600, L93
Gispert R., Lagache G., Puget J. L., 2000, A&A, 360, 1
Goto T. et al., 2010, A&A, 514, A6
Granato G. L., De Zotti G., Silva L., Bressan A., Danese L., 2004, ApJ, 600, 580
Griffin M. J. et al., 2010, A&A, 518, L3
Gruppioni C. et al., 2010, A&A, 518, L27
Hatziminaoglou E., Fritz J., Jarrett T. H., 2009, MNRAS, 399, 1206
Hatziminaoglou E. et al., 2010, A&A, 518, L33
Hauser M. G. et al., 1998, ApJ, 508, 25
Holland W. S. et al., 1999, MNRAS, 303, 659
Hughes D. H. et al., 1998, Nat, 394, 241
Huynh M. T., Frayer D. T., Mobasher B., Dickinson M., Chary R.-R., Morrison G., 2007, ApJ, 667, L9
Hwang H. S. et al., 2010, MNRAS, 409, 75
Ilbert O. et al., 2009, ApJ, 690, 1236
Iono D. et al., 2009, ApJ, 695, 1537
Ivison R. J. et al., 2010, MNRAS, 402, 245
Johnson H. L., 1966, ApJ, 143, 187
Kartaltepe J. S. et al., 2010a, ApJ, 709, 572
Kartaltepe J. S. et al., 2010b, ApJ, 721, 98
Kartaltepe J. S. et al., 2012, ApJ, 757, 23
Kennicutt R. C. Jr, 1998, ARA&A, 36, 189
Kessler M. F. et al., 1996, A&A, 315, L27
Kim D.-C., Sanders D. B., 1998, ApJS, 119, 41
Klaas U., Haas M., Heinrichsen I., Schulz B., 1997, A&A, 325, L21
Klaas U. et al., 2001, A&A, 379, 823
Kleinmann D. E., Low F. J., 1970, ApJ, 159, L165
Kovács A., Chapman S. C., Dowell C. D., Blain A. W., Ivison R. J., Smail I., Phillips T. G., 2006, ApJ, 650, 592
Krügel E., Siebenmorgen R., 1994, A&A, 282, 407
Lacy M. et al., 2004, ApJS, 154, 166
Lagache G., Puget J.-L., Dole H., 2005, ARA&A, 43, 727
Le Fevre O. et al., 2000, MNRAS, 311, 565

Le Floc'h E. et al., 2004, ApJS, 154, 170
Le Floc'h E. et al., 2005, ApJ, 632, 169
Le Floc'h E. et al., 2009, ApJ, 703, 222
Lilly S. J. et al., 2009, ApJS, 184, 218
Lisenfeld U., Isaak K. G., Hills R., 2000, MNRAS, 312, 433
Lotz J. M., Madau P., Giavalisco M., Primack J., Ferguson H. C., 2006, ApJ, 636, 592
Lotz J. M., Jonsson P., Cox T. J., Croton D., Primack J. R., Somerville R. S., Stewart K., 2011, ApJ, 742, 103
Low F. J., Tucker W. H., 1968, Phys. Rev. Lett., 21, 1538
Lutz D. et al., 1996, A&A, 315, L137
Lutz D., Spoon H. W. W., Rigopoulou D., Moorwood A. F. M., Genzel R., 1998, ApJ, 505, L103
Lutz D., Yan L., Armus L., Helou G., Tacconi L. J., Genzel R., Baker A. J., 2005, ApJ, 632, L13
Lutz D. et al., 2011, A&A, 532, A90
Magdis G. E. et al., 2010, MNRAS, 409, 22
Magdis G. E. et al., 2011, A&A, 534, 15
Magdis G. E. et al., 2012, ApJ, 760, 6
Magnelli B., Elbaz D., Chary R. R., Dickinson M., Le Borgne D., Frayer D. T., Willmer C. N. A., 2009, A&A, 496, 57
Magnelli B. et al., 2010, A&A, 518, L28
Magnelli B. et al., 2012, A&A, 539, A155
Michałowski M. J., Hjorth J., Castro Cerón J. M., Watson D., 2008, ApJ, 672, 817
Michałowski M., Hjorth J., Watson D., 2010, A&A, 514, A67
Moustakas L. A. et al., 2004, ApJ, 600, L131
Murakami H. et al., 2007, PASJ, 59, 369
Muzzin A., van Dokkum P., Kriek M., Labbé I., Cury I., Marchesini D., Franx M., 2010, ApJ, 725, 742
Narayanan D., Groppi C. E., Kulesa C. A., Walker C. K., 2005, ApJ, 630, 269
Neugebauer G. et al., 1984, ApJ, 278, L1
Nguyen H. T. O., 2010, A&A, 518, L5
Nordon R. et al., 2012, ApJ, 745, 182
Oliver S. J. et al., 2012, MNRAS, 424, 1614
Page M. J. et al., 2012, Nat, 485, 213
Pannella M. et al., 2009, ApJ, 698, L116
Papadopoulos P. P., Isaak K., van der Werf P., 2010, ApJ, 711, 757
Patel H. et al., 2011, MNRAS, 415, 1738
Pilbratt G. L. et al., 2010, A&A, 518, L1
Planck Collaboration, 2011, A&A, 536, A16
Poglitsch A. et al., 2010, A&A, 518, L2
Pope A. et al., 2006, MNRAS, 370, 1185
Pozzi F. et al., 2012, MNRAS, 423, 1909
Ptak A., Heckman T., Levenson N. A., Weaver K., Strickland D., 2003, ApJ, 592, 782
Puget J.-L., Abergel A., Bernard J.-P., Boulanger F., Burton W. B., Desert F.-X., Hartmann D., 1996, A&A, 308, L5
Reddy N. A., Steidel C. C., Fadda D., Yan L., Pettini M., Shapley A. E., Erb D. K., Adelberger K. L., 2006, ApJ, 644, 792
Reddy N. A., Erb D. K., Pettini M., Steidel C. C., Shapley A. E., 2010, ApJ, 712, 1070
Rieke G. H., Alonso-Herrero A., Weiner B. J., Pérez-González P. G., Blaylock M., Donley J. L., Marcillac D., 2009, ApJ, 692, 556
Rodighiero G. et al., 2010, A&A, 518, L25
Rosario D. J. et al., 2012, A&A, 545, A45
Roseboom I. G. et al., 2010, MNRAS, 409, 48
Roseboom I. G. et al., 2012, MNRAS, 419, 2758
Rowan-Robinson M. et al., 1997, MNRAS, 289, 490
Rowan-Robinson M. et al., 2005, AJ, 129, 1183
Rowan-Robinson M. et al., 2010, MNRAS, 409, 2
Rujopakarn W., Rieke G. H., Eisenstein D. J., Juneau S., 2011, ApJ, 726, 93
Salvato M. et al., 2009, ApJ, 690, 1250
Salvato M. et al., 2011, ApJ, 742, 61
Sanders D. B., Mirabel I. F., 1996, ARA&A, 34, 749
Sanders D. B. et al., 2007, ApJS, 172, 86
Santini P. et al., 2009, A&A, 504, 751
Santini P. et al., 2010, A&A, 518, L154
Schinnerer E. et al., 2008, ApJ, 689, L5
Scoville N. et al., 2007, ApJS, 172, 1
Seymour N., Symeonidis M., Page M. J., Huynh M., Dwelly T., McHardy I. M., Rieke G., 2010, MNRAS, 402, 2666
Seymour N. et al., 2011, MNRAS, 413, 1777
Shapley A. E., 2011, ARA&A, 49, 525
Siebenmorgen R., Krügel E., 2007, A&A, 461, 445 (SK07)
Silva L. et al., 1998, ApJ, 509, 103
Smith D. J. B. et al., 2012, MNRAS, 427, 703
Soifer B. T. et al., 1984a, ApJ, 278, L71
Soifer B. T. et al., 1984b, ApJ, 283, L1
Soifer B. T. et al., 2001, AJ, 122, 1213
Somerville R. S., Hopkins P. F., Cox T. J., Robertson B. E., Hernquist L., 2008, MNRAS, 391, 481
Stern D. et al., 2005, ApJ, 631, 163
Sturm E. et al., 2010, A&A, 518, L36
Symeonidis M., Willner S. P., Rigopoulou D., Huang J.-S., Fazio G. G., Jarvis M. J., 2008, MNRAS, 385, 1015
Symeonidis M. et al., 2009, MNRAS, 397, 1728
Symeonidis M., Rosario D., Georgakakis A., Harker J., Laird E. S., Page M. J., Willmer C. N. A., 2010, MNRAS, 403, 1474
Symeonidis M., Page M. J., Seymour N., 2011a, MNRAS, 411, 983
Symeonidis M. et al., 2011b, MNRAS, 417, 2239
Tacconi L. J. et al., 2006, ApJ, 640, 228
Tacconi L. J. et al., 2010, Nat, 463, 781
Takeuchi T. T., Buat V., Burgarella D., 2005, A&A, 440, L17
Valiante E., Lutz D., Sturm E., Genzel R., Tacconi L. J., Lehnert M. D., Baker A. J., 2007, ApJ, 660, 1060
Vega O., Clemens M. S., Bressan A., Granato G. L., Silva L., Panuzzo P., 2008, A&A, 484, 631
Werner M. W. et al., 2004, ApJS, 154, 1
Whitaker K. E., van Dokkum P. G., Brammer G., Franx M., 2012, ApJ, 754, L29
Wuyts S. et al., 2011, ApJ, 742, 96
Yun M. S. et al., 2008, MNRAS, 389, 333
Zahid H. J., Yates R. M., Kewley L. J., Kudritzki R. P., 2013, ApJ, 763, 92
Zamojski M., Yan L., Dasyra K., Sajina A., Surace J., Heckman T., Helou G., 2011, ApJ, 730, 125

APPENDIX A: REDSHIFTS

Here we examine the reliability of the photometric redshift catalogues used in this work (see Section 2.2) for sources which satisfy the initial criterion for the selection of our sample (Section 2.1): 24 μm sources that have detections (at least 3σ) at [100 and 160 μm] OR [160 and 250 μm].

For GOODS-N, we use the redshift catalogue of Berta et al. (2011) which includes spectroscopic redshifts assembled from various sources and photometric redshifts compiled using the EAZY code (Brammer et al. 2008) and up to 14 photometric bands. Berta et al. (2011) note that the fraction of outliers, defined as objects having $z_{\rm spec} - z_{\rm phot}/(1+z_{\rm spec}) > 0.2$, is about 2 per cent for sources with a PACS detection. For more details, we refer the reader to Berta et al. (2011). In Fig. A1 (top-panel), we compare the photometric and spectroscopic redshifts for the GOODS-N sample, indicating the 10 and 20 per cent uncertainty regions. There is excellent agreement in the redshifts.

For GOODS-S, we use the MUSYC redshift catalogue of Cardamone et al. (2010), complemented with the MUSIC redshift catalogue of Santini et al. (2009). Most redshifts come from Cardamone et al. (2010) with the addition of some from Santini et al. (2009). The Cardamone et al. (2010) photometric redshifts are compiled

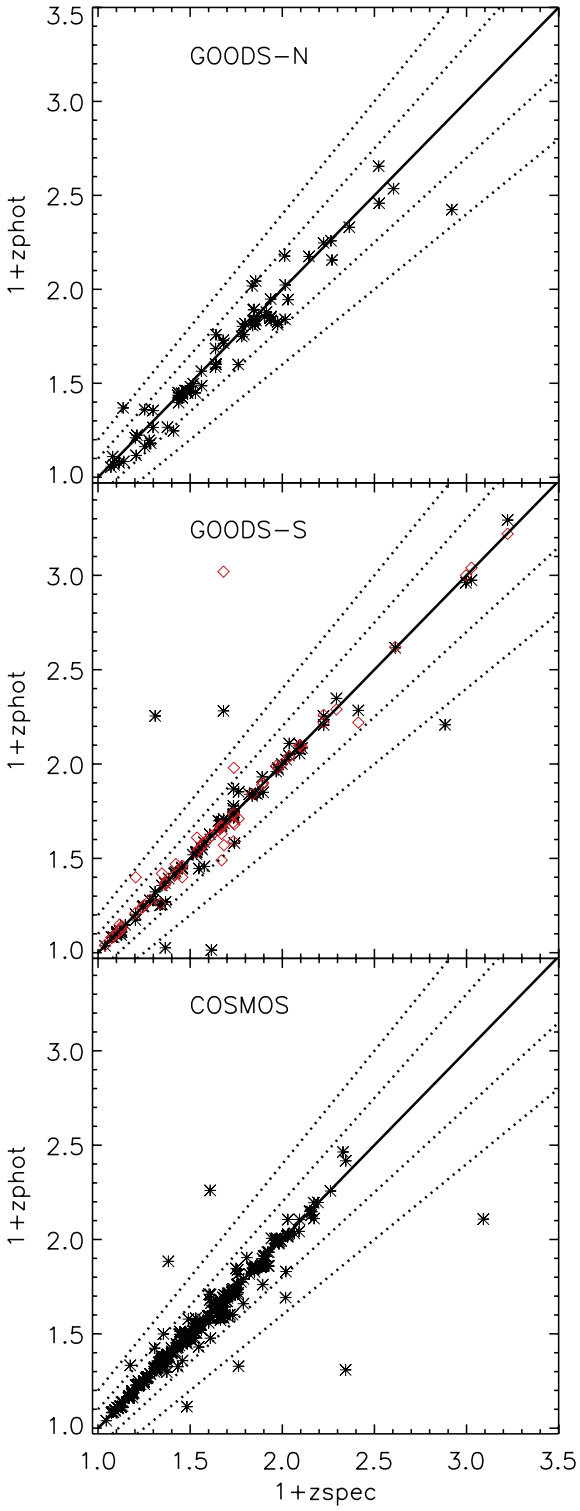

Figure A1. Comparison of spectroscopic and photometric redshifts for sources in the GOODS-N, GOODS-S and COSMOS samples which satisfy the initial criterion for the selection of our sample (Section 2.1): 24 μm sources that have detections (at least 3σ) at [100 and 160 μm] OR [160 and 250 μm]. The inner dotted lines denote the 10 per cent boundaries and the outer dotted lines denote the 20 per cent boundaries. In the middle panel, the asterisks mark the Cardamone et al. (2010) photometric redshifts and the diamonds the Santini et al. (2009) photometric redshifts.

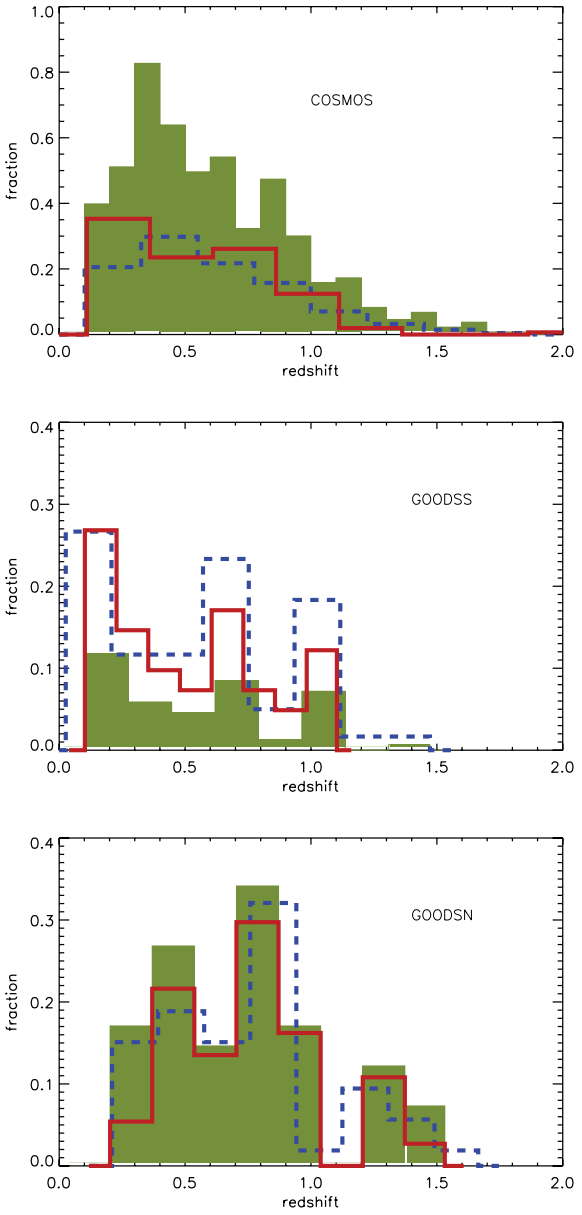

Figure A2. The redshift distribution of the final *Herschel* sample used in this work in COSMOS, GOODS-S and GOODS-N. The filled-in histogram shows the total redshift distribution, whereas the red histogram represents the spectroscopic redshifts and the blue dashed histogram the photometric redshifts.

using up to 28 photometric bands and the EAZY code (Brammer et al. 2008), resulting to high accuracy $z_{\rm spec} - z_{\rm phot}/(1 + z_{\rm spec}) \sim 0.00822$ out to high redshift. For more details, we refer the reader to the Cardamone et al. (2010) paper. Fig. A1 (middle panel) shows a comparison of photometric to spectroscopic redshifts for the sources in the GOODS-S sample for both Santini et al. (2009) and Cardamone et al. (2010) catalogues. There is excellent agreement between the spectroscopic and photometric redshift in both catalogues, with the catastrophic failures, which we define as a more than 20 per cent offset in $(1+z)$, being <1 per cent of the spectroscopic sample.

For COSMOS, the spectroscopic redshifts are from Lilly et al. (2009) and the photometric redshifts from Ilbert et al. (2009), derived using up to 30 photometric bands. The estimated accuracy of a median $z_{\rm spec} - z_{\rm phot}/(1 + z_{\rm spec}) = 0.007$ for the galaxies brighter

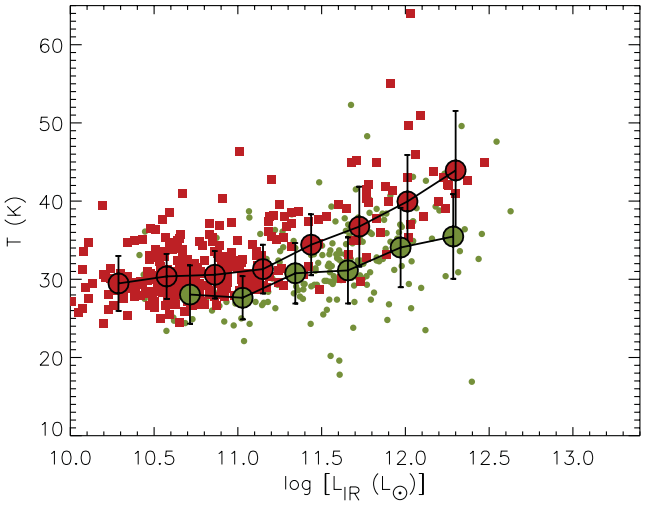

Figure A3. This figure is reproduced from the main part of the paper, but solely with spectroscopic redshifts. We see that the overall results remain the same; however, the statistics are reduced.

than $i = 22.5$. For the sources which host X-ray detected AGN, we substitute the Ilbert et al. redshift with a photometric redshift from Salvato et al. (2009, 2011). These are derived with a combination of AGN and galaxy templates and are hence more accurate for galaxies hosting AGN. Fig. A1 (lower panel) shows a comparison of photometric to spectroscopic redshifts for the COSMOS sample sources. The agreement is again excellent, with only about 1 per cent of sources outside the 20 per cent uncertainty region.

We next examine the redshift distribution of our final *Herschel* sample used in this work assembled in Section 5. This is shown in Fig. A2 for the three fields. Note that the photometric and spectroscopic redshift distributions agree, although the photometric redshift distribution tails off to higher redshifts. We examine whether the use of photometric redshifts would have any effect on our results, by reproducing one of our main figures using only spectroscopic redshifts (Fig. A3). We see that using only spectroscopic redshifts does not change the overall differences we find between the *Herschel* and local sample; however, it does significantly reduce the statistics.

This paper has been typeset from a TEX/LATEX file prepared by the author.